Northern Hemisphere Winter Blocking: Differing Onset Mechanisms across Regions

DOUGLAS E. MILLER[a] AND ZHUO WANG[a]

[a] *University of Illinois at Urbana–Champaign, Urbana, Illinois*

(Manuscript received 16 April 2021, in final form 17 December 2021)

ABSTRACT: Atmospheric blocking is a prolific producer of extreme weather with significant socioeconomic impacts. Different physical mechanisms for blocking onset have been proposed and are generally focused on two sectors: the Eurasian and the North Pacific. Here, we objectively separate blocking into four regions and investigate how the blocking onset mechanisms vary from one region to another, focusing on three factors: scale interactions between three frequency bands, Rossby wave breaking (RWB), and diabatic heating. Atlantic blocks are dominated by the low-frequency flow evolution that resembles the negative phase of the North Atlantic Oscillation and are influenced by cyclonic RWB toward the western edge of the anticyclone. Europe blocks are influenced by high-frequency, traveling waves across the Atlantic Ocean and develop rapidly, mainly attributed to strong anticyclonic RWB and interaction between high- and intermediate-frequency flow components. Asian blocks are fixated within a stationary wave train that spans upstream to the western Atlantic Ocean and do not have strong potential vorticity or RWB features. The Pacific blocks are mainly influenced by an intermediate-frequency retrograding wave train, while a low-frequency component resembling the Pacific–North American pattern is evident. The Pacific blocks also contain precursor signals in the stratosphere. Backward trajectory analysis revealed that 35%–45% of parcels initialized within the Atlantic, Europe, and Pacific blocking anticyclones experience heating and ascent, while adiabatic processes dominate Asian blocking. Overall, our analysis demonstrates the importance of decomposing the flow into three frequency bands and illustrates different blocking onset mechanisms over four sectors.

KEYWORDS: Northern Hemisphere; Blocking; Dynamics; Anticyclones; Winter/cool season

1. Introduction

Extreme weather events, such as floods, droughts, heatwaves, cold-air outbreaks, and extended severe weather periods, often result from atmospheric blocking events (Sillmann and Croci-Mospoli 2009; Buehler et al. 2011; Dole et al. 2011; Matsueda 2011; Sillmann et al. 2011; Miller et al. 2020, 2021). An atmospheric block is a synoptic-scale feature lasting days to weeks that halts the eastward movement of midlatitude weather systems (Rex 1950). The quasi-stationary, high pressure system causes the usual westerly flow to displace northward or split and can reverse the zonal flow along the storm track.

Several mechanisms have been proposed for the onset of atmospheric blocking events, which can be broadly grouped into planetary and local theories (Tyrlis and Hoskins 2008). Planetary theories emphasize large-scale Rossby wave dynamics (Austin 1980) excited by tropical precipitation anomalies (Cassou et al. 2005; Henderson et al. 2016), extratropical sea surface temperatures (SST; Peings and Magnusdottir 2014; O'Reilly et al. 2016), topographic forcing (Charney and DeVore 1979), or Rossby waves that arise solely due to internal atmospheric dynamics (Swanson 2001). Local theories include enhanced transient activity (Nakamura and Wallace 1990, 1993; Nakamura et al. 1997), the role of isentropic advection of low-potential-vorticity (PV) air (Nakamura 1994; Nakamura et al. 1997), and ascending low-PV air due to latent heat release during cloud formation (Pfahl et al. 2015; Steinfeld and Pfahl 2019). As reviewed in greater detail below, these mechanisms are not mutually exclusive as individual blocking events are unique, and the dominant mechanisms may vary for different regions (Nakamura et al. 1997; Drouard and Woollings 2018).

Studies in the early 1980s suggested that the interaction between baroclinic synoptic-scale waves and the planetary-scale waves is important in blocking initiation (Hansen and Chen 1982; Reinhold and Pierrehumbert 1982) and that repeated interaction can enhance blocking maintenance (Shutts 1983; Illari 1984; Hansen and Sutera 1993). Nakamura and Wallace (1990) showed that high-frequency fluctuations upstream, primarily in the form of strong cyclogenesis (Colucci 1985), play an important role in blocking formation over the eastern oceans. Upstream cyclones play a role in PV and warm temperature advection, leading to the increase of geopotential height in the area of blocking development. Colucci and Alberta (1996) found that the probability of Pacific and Atlantic blocking increased significantly relative to climatology within 60° longitude of explosive cyclogenesis. Lupo and Smith (1995) demonstrated that all 63 blocking anticyclones analyzed during 1985–88 were associated with antecedent cyclogenesis, half of which could be characterized as explosive development.

Nakamura et al. (1997) examined the role of high- and low-frequency flow in blocking formation over Europe and the North Pacific. They found that blocking events would fail to form without high transient activity over the North Pacific, while Europe blocking would still occur due to the presence of strong low-frequency perturbations. Luo (2005) emphasized the importance of the interaction between synoptic-scale eddies and suggested that topography plays a secondary role

Supplemental information related to this paper is available at the Journals Online website: https://doi.org/10.1175/JAS-D-21-0104.s1.

Corresponding author: Douglas E. Miller, dmiller23@niu.edu

DOI: 10.1175/JAS-D-21-0104.1

in initiating blocking development. More recently, Drouard and Woollings (2018) provided evidence for different mechanisms over three Eurasian sectors during the summer season. The results were consistent with Nakamura et al. (1997), which suggested that both high- and low-frequency dynamics were important over western Europe. Additionally, they showed that low-frequency dynamics are more important over western Russia. Nakamura and Huang (2018) compared blocking to a traffic jam on a highway, suggesting that the buildup of wave activity flux (WAF) due to some forcing upstream (e.g., cyclogenesis) may cause the WAF capacity of the jet to be exceeded and induce blocking onset. Later, Luo and Zhang (2020) found that the eddy-induced WAF reduces the divergence of the linear WAF upstream of a developing blocking anticyclone and favors blocking growth. These theories are consistent with previous findings, especially Nakamura (1994), that weakened westerlies lead to WAF accumulation.

The overturning of PV on an isentropic surface is associated with blocking formation. Low-PV air is advected from the subtropics poleward and is often associated with an anomalous anticyclonic circulation (Hoskins et al. 1985). Hoskins (1997) and Pelly and Hoskins (2003) introduced the mechanism of poleward intrusions of lower PV air on an isentropic surface for blocking formation. The amplitude of this "Rossby wave intrusion" may be large enough to induce irreversible overturning of PV contours and lead to the development of an anticyclonic circulation cut off from its origin and the onset of an atmospheric blocking event. This overturning is known as Rossby wave breaking (RWB) and is characterized by the irreversible overturning of PV contours on an isentropic surface or overturning of potential temperature on a PV surface (McIntyre and Palmer 1983).

The above mechanisms emphasize dry dynamics, but there is also evidence of diabatic influences. Diabatic heating associated with a cyclone's warm conveyer belt (WCB; Joos and Wernli 2012) can alter the PV structure, such that PV is reduced (increased) above (below) the diabatic heating maxima (Wernli and Davies 1997). The outflow of a WCB can significantly alter the upper-level PV pattern and amplify upper-level ridges, which modify the large-scale circulation (Stoelinga 1996; Pomroy and Thorpe 2000). Pfahl et al. (2015) demonstrated the importance of diabatic processes in blocking formation. Using backward trajectory analysis, they noted that 69% of trajectories were associated with a potential temperature increase of greater than 2 K (some cases greater than 25 K) when traced back to 7 days and concluded that the diabatic processes are of first-order importance in blocking formation. A recent study (Steinfeld and Pfahl 2019) discussed the differences in the impacts of diabatic heating based on blocking location and found that blocks located downstream of baroclinic development (i.e., Atlantic and Pacific jets) were more influenced by latent heating than blocks over land (Asia).

The purpose of this study is to examine how the winter blocking onset mechanisms vary from one region to another with a focus on the roles of multiscale interaction, Rossby wave breaking, and diabatic heating. Past studies tend to separate the low-frequency flow from the synoptic-scale eddies when analyzing multiscale interaction. Here, the importance of decomposing the anomalous flow into three frequency bands (low, intermediate, and high) is presented for blocking development across four sectors: Atlantic, Europe, Asia, and Pacific. Section 2 presents the data and methodology, including the blocking and RWB identification methods, sector identification, frequency decomposition analysis, and PV diagnostics. The blocking structure over the four sectors is examined in section 3, followed by an evaluation of the dynamical mechanisms in section 4. Section 5 contains the discussion and conclusions.

2. Methodology

a. Data

Most of the analysis is performed using the European Centre for Medium-Range Weather Forecasts (ECMWF) interim reanalysis (ERA-Interim, hereafter ERAI; ECMWF 2009; Dee et al. 2011) dataset during the winter season (DJF) from 1979/80 to 2016/17. Geopotential height at various pressure levels is used in this study. Zonal and meridional winds at 200-hPa (U200, V200) and PV at the 200-hPa level are used to investigate the PV budget during block formation. PV on the 350-K isentropic level is used to identify RWB. Two-meter temperature is used to calculate extreme temperature, as Miller and Wang (2019a). Extreme temperatures are defined as detrended daily temperatures greater (less) than the 90th (10th)-percentile temperatures for all DJF at each grid point, following removal of the seasonal cycle. Data are available on a T255L60 (~0.7° in horizontal) grid and were interpolated to a 1° latitude–longitude grid. PV350 on a 2.5° × 2.5° grid mesh is used for RWB detection (see section 2c). Anomalies are constructed by first removing long-term daily means on each calendar day, then removing the long-term trend.

b. Blocking identification

In early studies, blocking was identified as an anomalous high along the storm track that displaces the westerly flow northward (Lejenäs and Økland 1983; Tibaldi and Molteni 1990). Pelly and Hoskins (2003) advocated the PV perspective and identified blocking as a large-scale reversal of the meridional potential temperature gradient on a PV surface along the storm track. This method was later expanded to two dimensions to include blocks away from the storm track axis (Masato et al. 2012). Masato et al. (2013) followed the same methodology but used Z500 instead of potential temperature on the 2-PVU surface. They concluded that Z500 produced a similar climatology to that of potential temperature, and this method was later used by various studies (Kitano and Yamada 2016; Miller and Wang 2019a). Here, we follow the same method in blocking identification.

First, a central blocking latitude (CBL; Pelly and Hoskins 2003) was determined by removing a 5-day running mean from the daily average Z500 field, taking the standard deviation across one season, and finding the latitude of the maximum standard deviation per longitude. A 9° moving average is taken to ensure smooth changes between longitudes.

A blocking index (BI) was calculated daily at each longitude along the climatological CBL and is defined as

$$\mathrm{BI} = \frac{2}{\Delta\phi}\int_{\phi_o}^{\phi_n} Z_{500}\, d\phi \;-\; \frac{2}{\Delta\phi}\int_{\phi_s}^{\phi_o} Z_{500} d\phi, \qquad \mathrm{BI} > 0 \tag{1}$$

where ϕ_o is the CBL, ϕ_n is 15° north of the CBL, ϕ_s is 15° south of the CBL, and $\Delta\phi$ is 30°. If greater than zero, the blocking index implies a longitude is blocked [instantaneously blocked longitude (IBL); Barnes et al. 2012]. A group of IBLs (i.e., GIBL) exists if at least 15 consecutive degrees in longitude are blocked (large-scale), and a block only occurs if the group persists for at least 5 days and remains within 45° longitude from its original position (quasi-stationary). The blocking onset day is the first day when a GIBL meets blocking requirements (persist for at least 5 days and is quasi stationary). Masato et al. (2013) mentioned that the method identifies blocking highs and cutoff lows that divert the normal westerly flow.

c. *Rossby wave breaking identification*

The RWB detection algorithm described in Strong and Magnusdottir (2008) is used to identify RWB. The algorithm searches for high- or low-PV tongues associated with the overturning of PV circumpolar contours. RWB is often associated with the overturning of more than one PV contour. The algorithm performs redundancy control on each break and retains the PV contour representing the largest PV tongue area, defined as the PV level of RWB. The algorithm stores various parameters, such as RWB location, time, PV level, and orientation (cyclonic or anticyclonic). This algorithm can be applied to different isentropic levels. Six-hourly PV at the 350-K level (PV350) is used as this is the approximate pressure level (~200 hPa) of the PV minima of the blocks (not shown). In section 4, the location of RWBs within 3 days of blocking onset is presented by highlighting the grid points involved in a RWB, which are those grid points located within a low-PV tongue relevant to blocking formation.

d. *Identification of blocking sectors*

The blocking index described in section 2b allows for spatial and temporal characterization of atmospheric blocking events. Figure 1a shows the long-term mean of blocking frequency (average number of days per winter season when a longitude is involved in a block). The long-term mean of the blocks contains two primary peaks, one over Eurasia and the other over the Pacific, and a secondary peak located around 100°E (Fig. 1a). The secondary peak appears in various studies that analyzed 1D blocking frequency (Pelly and Hoskins 2003; Masato et al. 2012) but is absent from Masato et al. (2013). This may be due to the different periods analyzed. In fact, stark differences in blocking frequency at 100°E were discovered between 1979–2001 and 2002–17 (not shown). The standard deviation of blocking frequency also indicates a region of variability west of the primary peak. EOF analysis was applied to the 2D (time × longitude) daily time series of blocking occurrence to identify the dominant mode of blocking activity and to objectively identify blocking sectors. The

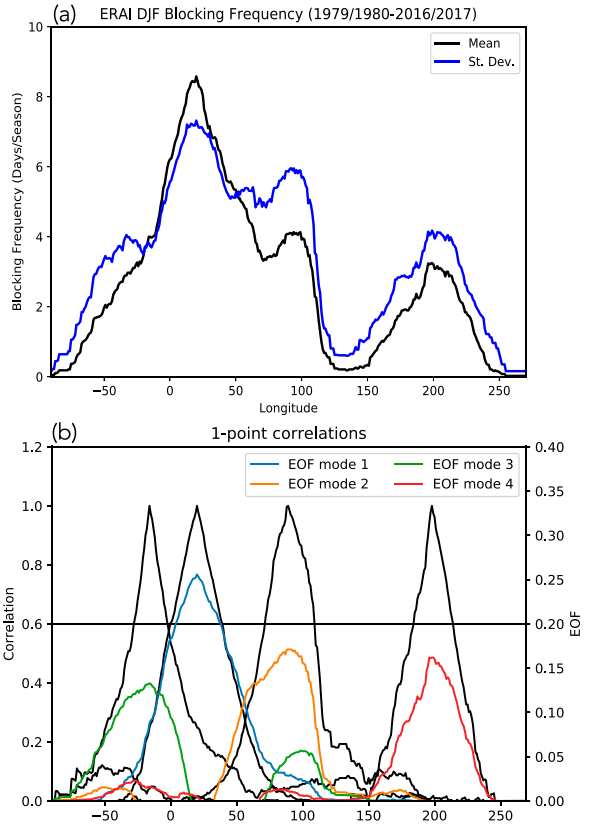

FIG. 1. (a) Long-term mean (black) and standard deviation (blue) of blocking frequency (days per DJF). (b) The four leading EOF modes for blocking frequency (colors). Black lines are one-point correlations of blocking frequency centered on the peaks of the four leading EOF modes. The horizontal black line represents the chosen correlation threshold to define blocking sectors.

first four modes, chosen using the elbow method (Kodinariya and Makwana 2013), explain 62% variance and roughly correspond to the four peaks in the standard deviation (Fig. 1a). The four modes (Fig. 1b) represent an Atlantic sector (EOF3; 11% variance), a Europe sector that is close in location to the primary peak (EOF1; 28% variance), an Asian sector (EOF2; 14% variance), and a Pacific sector (EOF4; 9% variance). To determine the longitude limits of each sector, one-point correlations of blocking frequency were calculated with the reference point set on the peak of each EOF. A cutoff correlation of 0.6 was subjectively chosen to separate the sectors and prevent overlap. The Atlantic sector (34°–2°W), the Europe sector (8°–40°E), the Asian sector (77°–104°E), and the Pacific sector (175°–146°W) contain 16, 40, 17, and 13 blocking events, respectively, over the winters of 1979/80 to 2016/17. Decreasing or increasing the threshold of 0.6 adds or removes a few events and does not substantially change the results of this study. Pattern correlations, or anomaly correlation coefficients (ACCs), and average variance are calculated over the blocking sectors throughout this study. The blocking sectors span the longitude ranges listed above and span from the CBL to 20° north of the CBL.

e. Backward trajectory analysis

The National Oceanic and Atmospheric Administration's (NOAA) Hybrid Single-Particle Lagrangian Integrated Trajectory model (HYSPLIT; Stein et al. 2015) was used to evaluate the role of diabatic heating in the different blocking sectors. A trajectory was released at 10 000 m above sea level (~200 hPa, or the approximate height of the tropospheric minimum PV anomaly, not shown) every degree of longitude spanning the blocking sector limits (see section 2d) and every degree of latitude spanning 15° north of the long-term mean CBL, which corresponds to the area of low-PV anomalies. The total number of parcels released per block is 403, 544, 448, and 496 parcels for the Atlantic, Europe, Asian, and Pacific blocks, respectively, yielding over 42 000 trajectories for all blocking events in this study. Due to the different blocking sector longitude ranges, different parcel quantities are released for different sectors. The trajectories were initialized on the blocking onset date, and the model was integrated backward for 72 h (3 days). The HYSPLIT model allows the potential temperature associated with the parcels to be documented along its trajectory.

f. Frequency analysis

Many studies (Nakamura and Wallace 1990, 1993; Nakamura et al. 1997; Drouard and Woollings 2018) decomposed the total flow into high- and low-frequency components (separated by a period of 6–8 days) when studying blocking mechanisms. Rennert and Wallace (2009) pointed out the limitations of the two-way decomposition. In particular, the low-frequency flow (>6–8 days) contains an assortment of different phenomena, including cutoff lows, propagating Rossby waves, and blocking anticyclones. Here, a total anomaly field with respect to the climatological seasonal cycle was decomposed into three frequency bands using a sixth-order Butterworth digital filter: high (≤6 days), intermediate (6 < period ≤ 30 days), and low (>30 days). Rennert and Wallace (2009) showed that the low- and intermediate-frequency bands are characterized by planetary-scale teleconnection patterns and Rossby wave trains oriented along a great circle route, respectively, while the high-frequency band is featured by eastward propagating baroclinic waves. This frequency decomposition is also broadly consistent with the flow decomposition by Luo et al. (2019) based on different spatial scales, as a higher-frequency flow component is typically associated with a smaller spatial scale.

To investigate the flow contributions to blocking onset, the variance of Z500 was calculated at each grid point every six hours for a frequency band as follows:

$$\mathrm{Var}\left[Z_i(t,x,y)\right] = \left[Z_i(t,x,y) - \overline{Z}_i(x,y)\right]^2, \tag{2}$$

where i denotes the different frequency bands; t is the time; $Z_i(t,x,y)$ is the 6-hourly 500-hPa geopotential height at longitude x and latitude y at time t; $\overline{Z}_i(x,y)$ is the DJF long-term mean from 1979/80 to 2016/17. Anomalies of the variance were then constructed by removing the long-term 6-hourly average variance for each frequency band on a given 6-hourly time step (i.e., removing the seasonal cycle). In our subsequent analysis, the variance anomalies were averaged over the corresponding blocking sectors for day −10 to day +5 (day 0 is the blocking onset time).

In addition to examining the average variance, the pattern correlation (Wilks 2011) was calculated over the blocking sector between the total Z500 anomaly field and each frequency band from day −10 through day 5. A large ACC indicates that a decomposed field has a similar spatial pattern as the total field, while the variance analysis shows the contribution to the total variance. It is important to state that the average variance and ACC help illustrate the direct contribution of different frequency bands to blocking development within the blocking sector but do not represent their contributions upstream of the blocking sector (e.g., Fig. 6). The upstream impacts of the frequency bands will be illustrated by the temporal evolution of the flow (i.e., movies S1–S4 in the online supplemental material).

g. Potential vorticity diagnostics

To investigate the role of multiscale interaction in blocking development, we employed the PV budget equation (Martin 2013):

$$\frac{\partial q}{\partial t} = -\nabla\cdot(\mathbf{V}q) - \frac{\partial \omega q}{\partial p} - g(\zeta+f)\frac{\partial \dot{\theta}}{\partial p} + R, \tag{3}$$

where q represents 200-hPa PV, $\mathbf{V}$ represents the 200-hPa horizontal wind vector, ω represents the vertical velocity, g represents gravity, ζ represents relative vorticity, f represents the Coriolis parameter, and $\partial\dot{\theta}/\partial p$ represents the change in the heating rate with pressure. The heating rate is the rate of change in θ between hour −72 and hour 0. The terms from left to right represent the local PV tendency, the convergence of the horizontal PV flux, the convergence of vertical PV flux, the PV production due to diabatic heating, and the residual term, which includes frictional effects and subgrid processes. Here, we focus on the PV tendency, the horizontal and vertical PV flux convergence, and the diabatic heating term over the 72 h before blocking onset.

To examine multiscale interactions, q is decomposed into four terms as discussed earlier:

$$q = q_c + q_{\mathrm{LF}} + q_{\mathrm{IF}} + q_{\mathrm{HF}}, \tag{4}$$

where the subscript c denotes the climatological seasonal cycle, while LF, IF, and HF represent the low-, intermediate-, and high-frequency components, respectively. A similar decomposition can be made for the horizontal velocity vector $\mathbf{V}$, and then the horizontal PV flux term can be expanded into 16 terms. It was found that the terms associated with the q_c or $\mathbf{V}_c$ are negligible compared to the other flux terms. We thus have the following approximation:

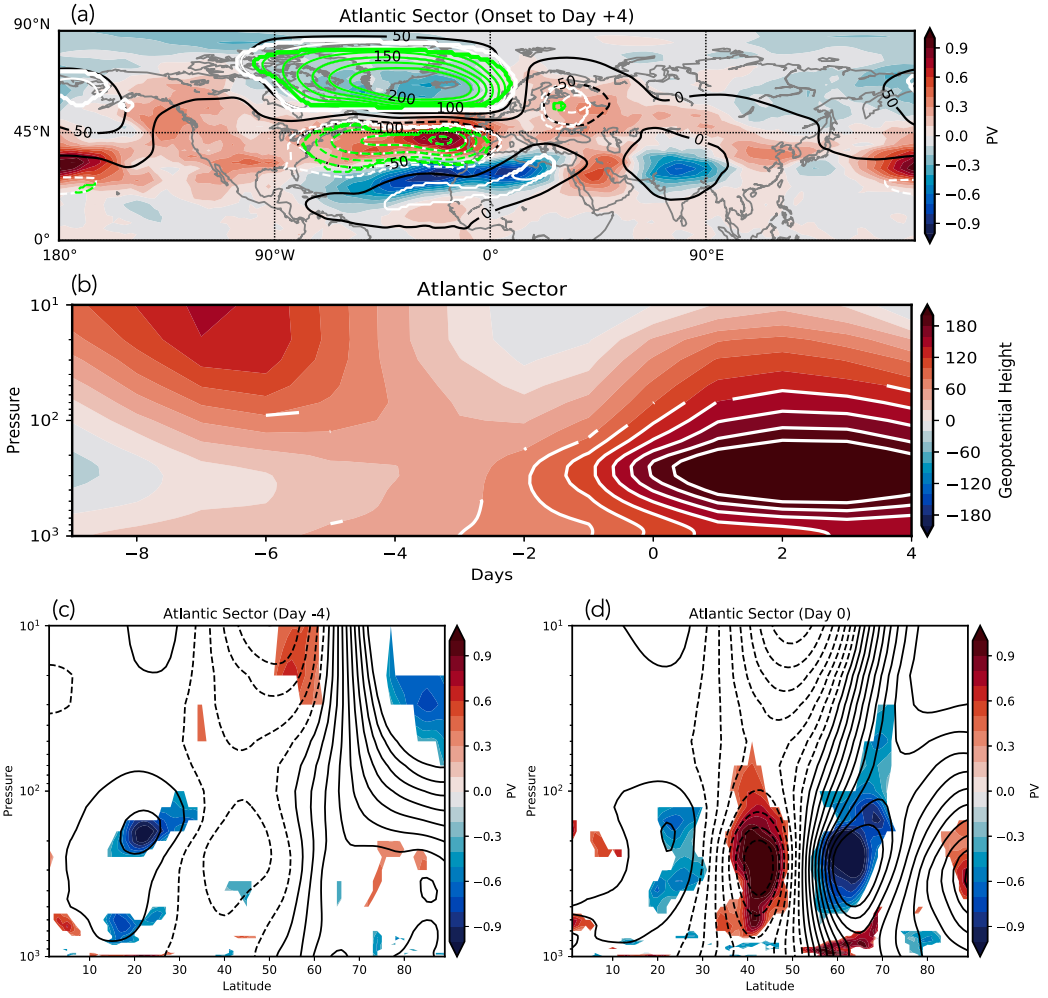

FIG. 2. (a) 5-day average (onset to day +4) of 500-hPa geopotential height (contours; m) and PV (shading; 1.0×10^{-6} m^2 s^{-1} K kg^{-1}) composite anomalies for the Atlantic sector blocking events. White contours indicate significant anomalies at the 95% level using a Student's t test, while green contours indicate field significant ($\alpha_{\mathrm{FDR}} = 0.1$) anomalies. (b) Time–height cross section of geopotential height anomalies over the blocking sector (55°–75°N, 34°–2°W). White contours indicate significant anomalies at the 95% level using a Student's t test. (c) Latitude–pressure level cross section (averaged over blocking sector longitude limits) of geopotential height anomalies (contours) and PV (color shading) for 4 days prior to blocking onset. Only significant PV anomalies are shown (95% level). (d) As in (c), but for the onset day.

$$\overline{\partial q/\partial t} \approx -\nabla\cdot\overline{\mathbf{V}_{\mathrm{LF}}q_{\mathrm{LF}}} - \nabla\cdot\overline{\mathbf{V}_{\mathrm{LF}}q_{\mathrm{IF}}} - \nabla\cdot\overline{\mathbf{V}_{\mathrm{LF}}q_{\mathrm{HF}}} - \nabla\cdot\overline{\mathbf{V}_{\mathrm{IF}}q_{\mathrm{LF}}} - \nabla\cdot\overline{\mathbf{V}_{\mathrm{IF}}q_{\mathrm{IF}}} - \nabla\cdot\overline{\mathbf{V}_{\mathrm{IF}}q_{\mathrm{HF}}}$$
$$- \nabla\cdot\overline{\mathbf{V}_{\mathrm{HF}}q_{\mathrm{LF}}} - \nabla\cdot\overline{\mathbf{V}_{\mathrm{HF}}q_{\mathrm{IF}}} - \nabla\cdot\overline{\mathbf{V}_{\mathrm{HF}}q_{\mathrm{HF}}} - \partial\overline{\omega q}/\partial p - \overline{g(\zeta+f)\frac{\partial\dot{\theta}}{\partial p}} + \overline{R}, \tag{5}$$

where the flow decomposition is only applied to the horizontal PV flux term in Eq. (3). Here we focus on the period before blocking onset, from day −3 to day 0. An overbar denotes an average over the 3 days and all blocking events in the sector of interest. The prime (′) terms in section 4 indicate the various anomalies from the seasonal cycle.

h. Statistical test

The two-tailed Student's t test was used to assess the significance of composite anomalies, with the null that the anomalies do not differ from zero. Results are significant if the p value is less than 0.05 or stated otherwise in the text. Field significance

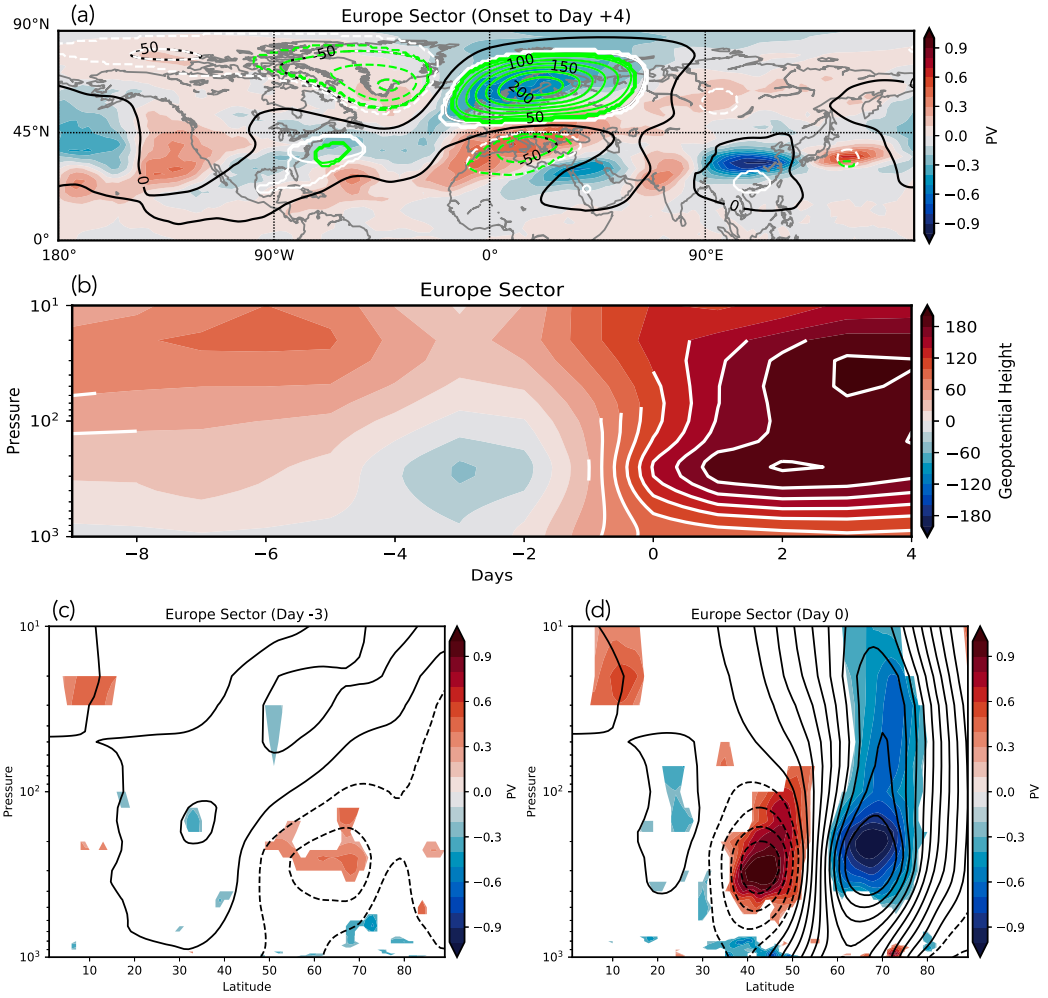

FIG. 3. As in Fig. 2, but for the Europe sector blocking events with the exception that (c) represents day −3. The blocking sector spans 50°–70°N, 8°–40°E.

was calculated using the false discovery rate (FDR), which requires a stronger significance threshold (Wilks 2016).

3. Evaluation of blocking structure

a. *Atlantic sector*

Figure 2a shows the composite Z500 and PV350 anomalies (blocking onset to day +4) for the Atlantic sector. The Atlantic sector blocks are characterized by a classic negative phased North Atlantic Oscillation (NAO; Hurrell et al. 2003). Field significant (α_{FDR} = 0.1) positive geopotential height anomalies are centered over Greenland extending from the Hudson Bay across the North Atlantic to the western portion of Scandinavia. Situated equatorward is the southern node of the NAO, which contains large areas of field significant negative height anomalies. PV anomalies of a similar pattern but opposite polarities are also found over the North Atlantic. The Atlantic blocks are associated with a significant increase in extreme warm temperature frequency over Greenland (within the blocking anticyclone) and a significant increase in extreme cold temperature frequency over the eastern United States and Europe (Fig. S1a). The blocking composites here agree with past studies that the negative NAO is associated with more frequent blocking occurrence (Benedict et al. 2004; Croci-Maspoli et al. 2007; Woollings et al. 2008; Davini et al. 2012).

Figure 2b displays the local evolution of geopotential height anomalies over the blocking sector. It demonstrates a gradual increase in geopotential height, where significant positive anomalies are evident several days before onset. Positive height anomalies descend from the stratosphere (although not significant) from day −9 to day −3, which could be related to sudden stratospheric warming (SSW) events that are known to influence the NAO (Scaife et al. 2005; Toniazzo and Scaife 2006; Ineson and Scaife 2009; Bell et al. 2009). In fact, significant positive Z70 anomalies are evident over the Arctic, representing a weakened stratospheric polar vortex (Fig. S2, top) 10 days before blocking onset, and is similar to the stratospheric configuration during NAO− winters (Miller and Wang 2019b). The deep NAO− structure is also evident

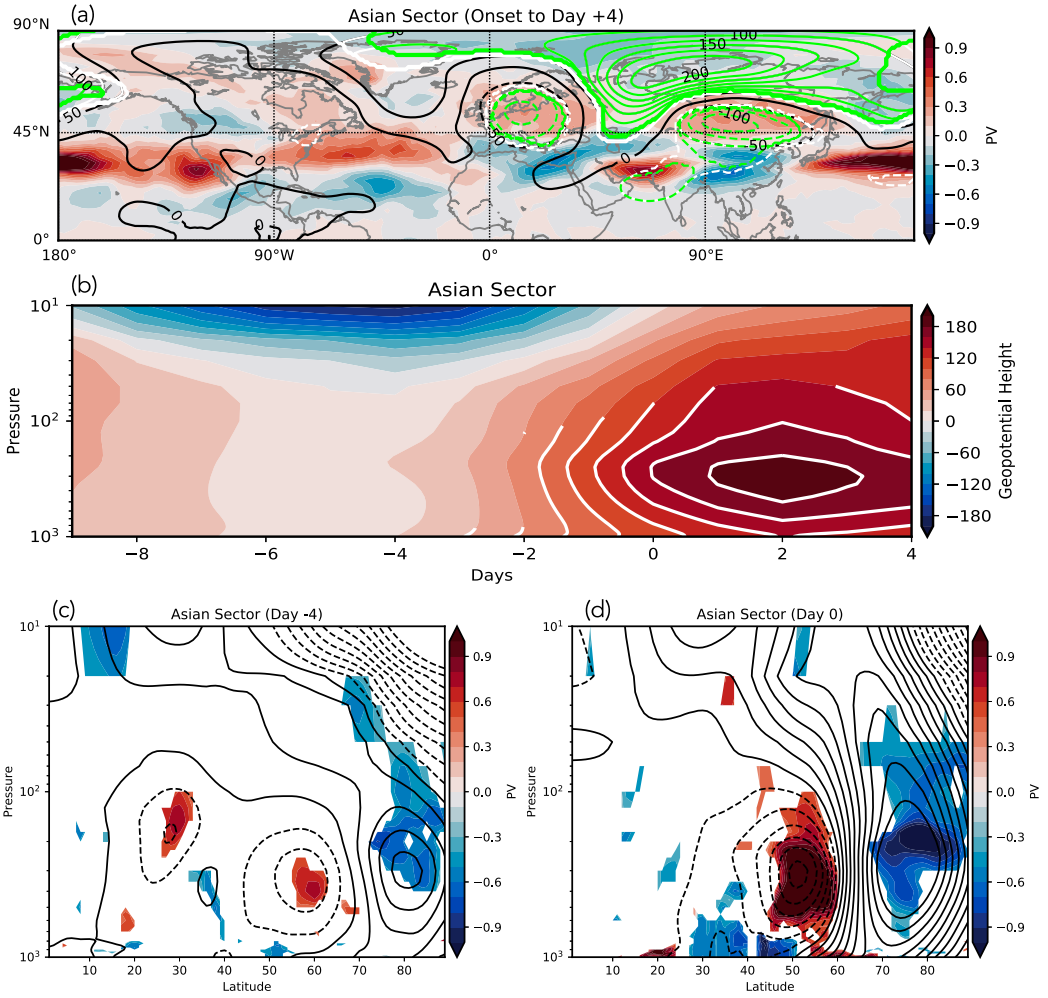

FIG. 4. As in Fig. 2, but for the Asia sector blocking events. The blocking sector spans 60°–80°N, 77°–104°E.

in the latitude–pressure cross sections (Figs. 2c,d), where strong positive height anomalies are seen in the stratosphere at day −4. The north–south dipole strengthens from day −4 to onset, and the positive height anomalies extend downward into the troposphere. The main PV anomalies associated with the NAO-like structure are located in the upper troposphere (300–200 hPa) centered around 40° and 60°N.

b. *Europe sector*

Blocking over the Europe sector is manifested as Scandinavian blocking (Fig. 3a) within a quadrupole structure. Field significant positive Z500 anomalies exist over Scandinavia with significant negative anomalies to the south, while a dipole-like anomaly pattern of the opposite polarity exists upstream. Collocated with the Z500 anomalies are PV anomalies of the opposite polarity and are reminiscent of a classic Rex-dipole block (Woollings et al. 2018). A significant increase in extreme warm temperature frequency is collocated within the blocking anticyclone poleward of Scandinavia, while an increase in extreme cold temperature frequency is collocated with the negative Z500 anomalies upstream and to the south of the blocking anticyclone (Fig. S1b).

Weak negative geopotential height anomalies in the troposphere to lower stratosphere precede Europe sector blocking onset, and positive anomalies rapidly develop within 2 days before blocking onset (Fig. 3b). The substantial change of the longitudinal averaged height and PV anomalies from day −3 to day 0 also illustrates the rapid onset of Europe blocking events. The height anomalies are much weaker, and significant PV anomalies are hardly discernable 3 days before onset (Fig. 3c), in contrast to the strong blocking high and associated negative PV anomalies at onset (Fig. 3d). As shown later in section 4, Rossby wave breaking plays a significant role in the onset of Europe blocking events. The strong influence by high- and intermediate-frequency PV flux interactions may contribute to the abruptness of the blocking onset in this sector.

c. *Asia sector*

Asian sector blocks are characterized by a circumglobal stationary wave pattern (Fig. 4a). In particular, field-significant

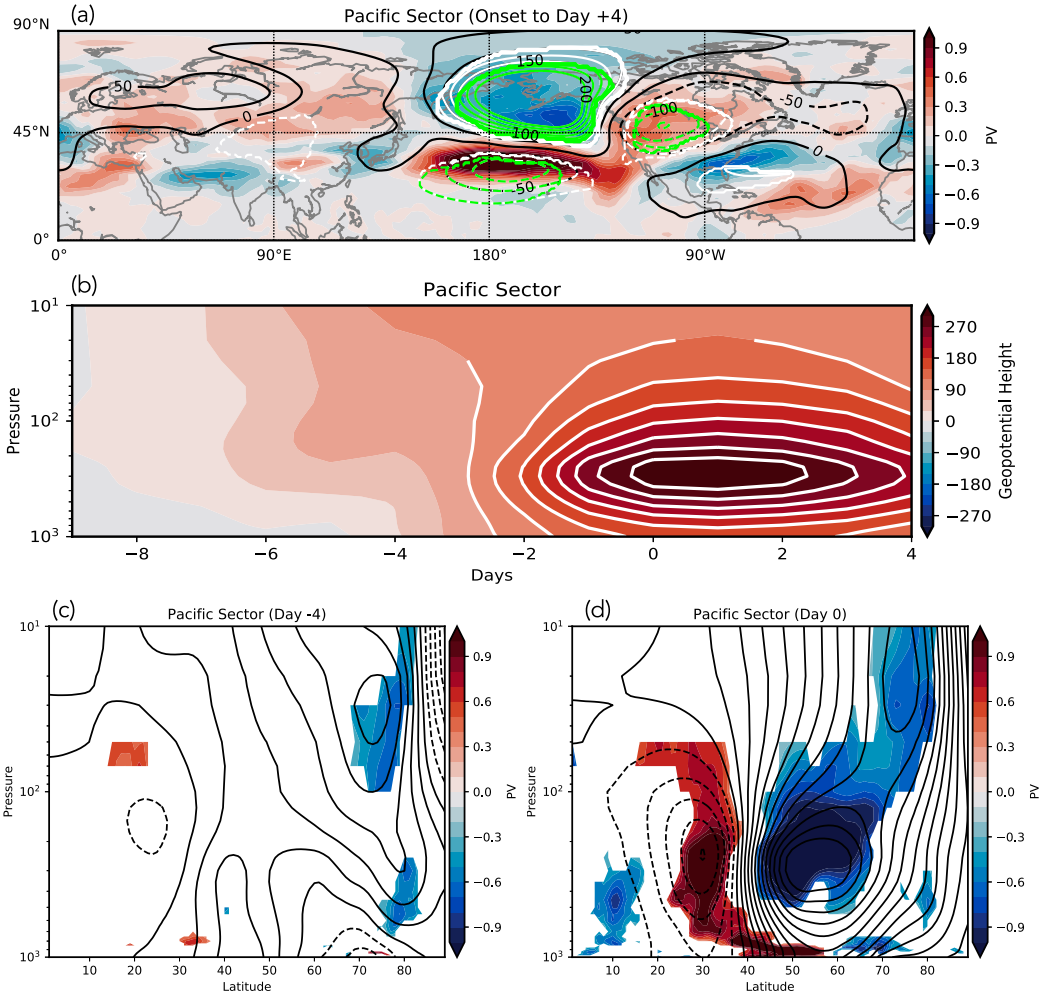

FIG. 5. As in Fig. 2, but for the Pacific sector blocking events. The blocking sector spans 45°–65°N, 175°–146°W.

positive anomalies are centered over Siberia, extending from the east coast of Scandinavia to the east coast of Asia, and negative anomalies are found south of the blocking sector over central Asia and Europe. Increases in extreme warm temperature frequency are located over the polar region north of Russia. In contrast, a strong and significant increase of extreme cold temperature frequency is situated just south of the blocking anticyclone, likely resulting from strong cold temperature advection (Fig. S1c). The anomalous cyclone upstream of the blocking high can be traced back to 9 days before onset developing off the coast of Europe, and the anomalous cyclone becomes strong as the center slowly shifts inland. The quasi-stationary nature of the wave train can be seen in Fig. S3.

Figure 4b reveals significant positive geopotential height anomalies over the Asian sector at day −3 which steadily strengthens throughout blocking development, displaying a deep blocking structure. Negative anomalies are present in the upper stratosphere before the blocking onset. Although Fig. 4b does not show significant height anomalies in the stratosphere before onset, significant negative PV anomalies are evident poleward of 70°N 4 days before onset in the lower stratosphere (Fig. 4c), and further examination of the Z70 anomalies indicate a displaced polar vortex over North America (Fig. S2). The anomalous high strengthens by onset and extends into the stratosphere with an equatorward vertical tilt (Fig. 4d).

d. *Pacific sector*

The Pacific sector blocks are characterized by a strong Alaskan ridge (Fig. 5a). Negative Z500 anomalies exist equatorward of the blocking high, and a downstream wave train spans across North America and extends to the subtropical Atlantic. However, wave signals are weak and most insignificant upstream of the blocking high, consistent with Nakamura et al. (1997). A significant increase in extreme warm temperature frequency is collocated with the blocking high, and extreme cold temperatures occur more frequently across the United States (Fig. S1d). Like the Atlantic and Asian blocks, there is a gradual buildup of geopotential height anomalies, and weak positive anomalies in the stratosphere show downward

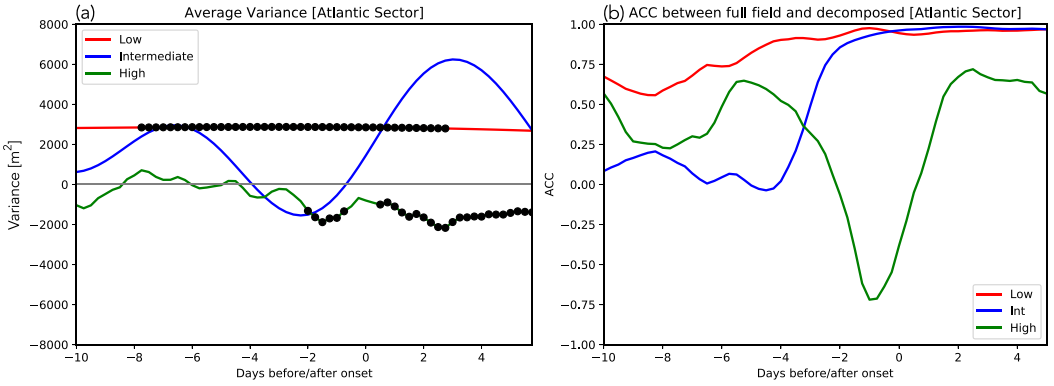

FIG. 6. (a) Average variance anomalies over the Atlantic blocking sector for the low- (red), intermediate- (blue), and high- (green) frequency components of Z500 from day −10 to day 5. Black circles indicate significant variance anomalies (95% confidence level). (b) The ACC between the full Z500 field and the low- (red), intermediate- (blue), and high- (green) frequency components of the Z500 field from day −10 to day 5.

propagation before blocking onset (Fig. 5b). At day −4 (Fig. 5c), the block is not developed in the troposphere, but significant negative PV anomalies and strong positive geopotential height anomalies exist in the stratosphere. At onset (Fig. 5d), the blocks strengthen, and significant negative PV anomalies extend from the middle troposphere throughout the stratosphere. Further analysis shows that the stratospheric polar vortex is displaced 10 days before the blocking onset. Significant positive Z70 anomalies are located over the North Pacific from day −5 to day 5 (Fig. S2), indicating the possible influence of stratospheric precursors on blocking development.

4. Physical mechanisms involved in blocking development

a. *Atlantic sector*

1) INVESTIGATION OF THE DECOMPOSED Z500 FIELD

The NAO evolves across different time scales (Hurrell and Deser 2010), such that we anticipate multiscale interaction in the development of Atlantic blocking events. First, we examine the decomposed Z500 height field and the associated variance over the blocking sector. Figure 6a shows the composite average variance anomalies from each frequency band from day −10 to day 5 for the Atlantic blocking events. Significant positive anomalies in low-frequency variance are evident from day −8 to day 3. The intermediate frequency experiences negative anomalies from day −4 to day −1 and above-average variance through day 5 of the blocking events, although nonsignificant. High-frequency variance anomalies are close to zero before day −2 and are significantly negative afterward, which is expected as the blocking high itself is a quasi-stationary feature.

Another way to assess the contribution of the different frequency bands is to examine the pattern correlation between the total Z500 field and each of the frequency components of Z500 (Fig. 6b). The large footprint of the low-frequency flow on the Z500 field is shown by large correlations (>0.6) throughout the period. The ACC of the intermediate flow is around 0.1 at day −10 and gradually increases through blocking onset. In contrast, the ACC of the high-frequency flow decreases after day −6 and is largely negative just before onset. The evolution of the low-frequency flow from day −10 to onset (movie S1) resembles the negative NAO, contributing to the strong positive ACC, while the high-frequency flow is characterized by eastward migrating weather patterns with a strong low anomaly developing west of the blocking anticyclone at day −1 to onset. The intermediate-frequency component of the flow resembles the positive phase of the NAO at day −10 and transitions to a NAO− pattern closer to onset, consistent with the increasing ACC close to blocking initiation in Fig. 6b. The NAO− signature evident in the low-frequency component of the flow indicates a weakened Atlantic jet, allowing for more frequent RWB and increased blocking occurrence (Woollings et al. 2008; Luo et al. 2019).

2) PV FLUX SCALE INTERACTION, RWB, AND DIABATIC HEATING

The importance of multiscale interaction in the formation of blocking anticyclones has been noted (Luo et al. 2014, 2019; Drouard and Woollings 2018; Nakamura and Huang 2018). To further investigate the role of multiscale interaction in different blocking sectors, we examine the local PV tendency, the total and decomposed 200-hPa horizontal PV flux fields and their convergence, the vertical PV flux convergence term, the diabatic heating term, and the location of RWB, within 3 days of blocking development.

Figure 7a displays the 3-day (day −3 to day −1) averaged local PV tendency and the location of anticyclonic and cyclonic RWB for the 72 h before onset. The PV tendency is largely negative just west of Scandinavia and is consistent with blocking development in the Atlantic sector (34°–2°W). The negative PV tendency is partly contributed by diabatic heating east of Iceland (Fig. 7c). Although horizontal PV-flux convergence is mixed with divergence in the region of negative PV tendency, PV-flux divergence occurs west near the center of the blocking anticyclone (Fig. 7b), where the NAO− feature is already

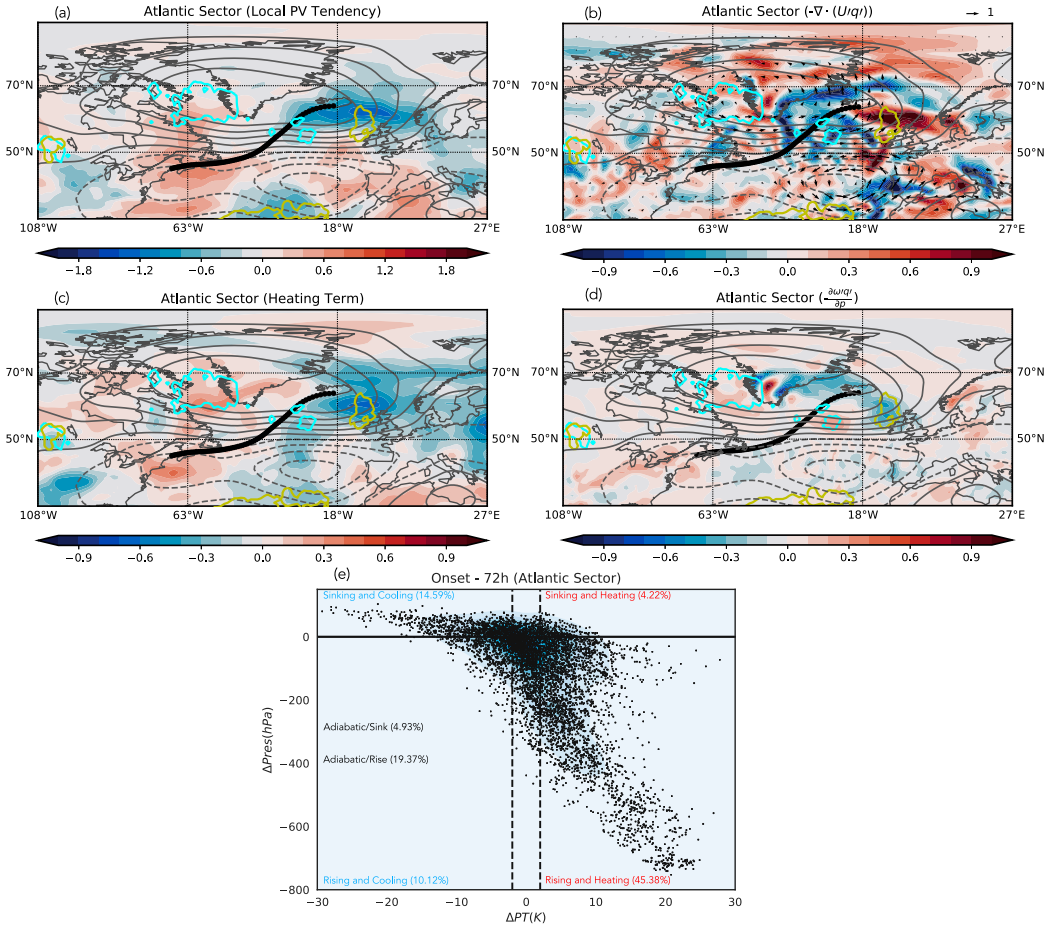

FIG. 7. (a) 200-hPa local PV tendency (shading; 10^{11} m^2 K s^{-2} kg^{-1}), Z500 anomalies (gray contours; from −100 to 100 m every 25 m), average trajectory path for all heated and ascending parcels (thick black contour), and locations of anticyclonic (yellow contours) and cyclonic (cyan contours) RWB within 3 days of Atlantic blocking development. (b) As in (a), but for 200-hPa horizontal PV flux ($U'q'$; vectors; 10^5 m^3 s^{-2} K kg^{-1}, scale in the top right) and PV flux convergence (shading; 10^{11} m^2 K s^{-2} kg^{-1}). (c) As in (a), but for the PV production by heating term (shading; 10^{11} m^2 K s^{-2} kg^{-1}). (d) As in (a), but for the vertical PV flux convergence term (shading; 10^{11} m^2 K s^{-2} kg^{-1}). (e) The change in potential temperature (K) vs the change in pressure (hPa) for backward trajectories between onset and 3 days prior. Above (below) the $y = 0$ line indicates parcels that experience overall descent (ascent). Diabatic cooling (heating) is less (greater) than −2 K (2 K), while in between represent adiabatic cases.

established. Contributions are also evident from vertical PV flux divergence in the blocking center (Fig. 7d), joining the horizontal PV flux divergence in blocking maintenance. A small area of anticyclonic RWB is evident near the negative PV tendency, while cyclonic RWB occurs upstream over the Labrador Sea. The poleward transport of lower-PV air associated with the cyclonic RWB may help build the anticyclone further west seen in movie S1, where the positive anomalies of intermediate-frequency Z500 strengthen in the NAO+ to NAO− transition. The enhanced cyclonic RWB is associated with equatorward PV fluxes, which agrees with previous findings that cyclonic RWB plays a crucial role in developing the NAO−, especially in the western Atlantic (Michel and Rivière 2011; Swenson and Straus 2017).

The role of diabatic heating in blocking development (Fig. 7c) is consistent with previous studies (Pfahl et al. 2015; Steinfeld and Pfahl 2019; Yamamoto et al. 2021). The contribution of diabatic processes is further investigated by examining the potential temperature change along parcel trajectories within 3 days before blocking onset. Backward trajectory analysis reveals that a large percentage (45%) of parcels experience ascent and heating of more than 2 K (some greater than 25 K) within 3 days before blocking onset (Fig. 7e). The average path of heated and ascending parcels (Fig. 7a) originates from the east coast of North America and shows a cyclonic curvature first and then an anticyclonic curvature. Of the ~2700 parcels that experience heating and ascent, 610 parcels (~22% of heating and ascending parcels, or 10.1% of total parcels) are associated with ascent of more than 400 hPa. It indicates that the warm-conveyer belt may play a role in blocking formation over the Atlantic (Pfahl et al. 2015; Steinfeld and Pfahl 2019). The parcels which experience ascent of more than 400 hPa (not shown) originate much further south (~30°N), consistent with higher water vapor content in

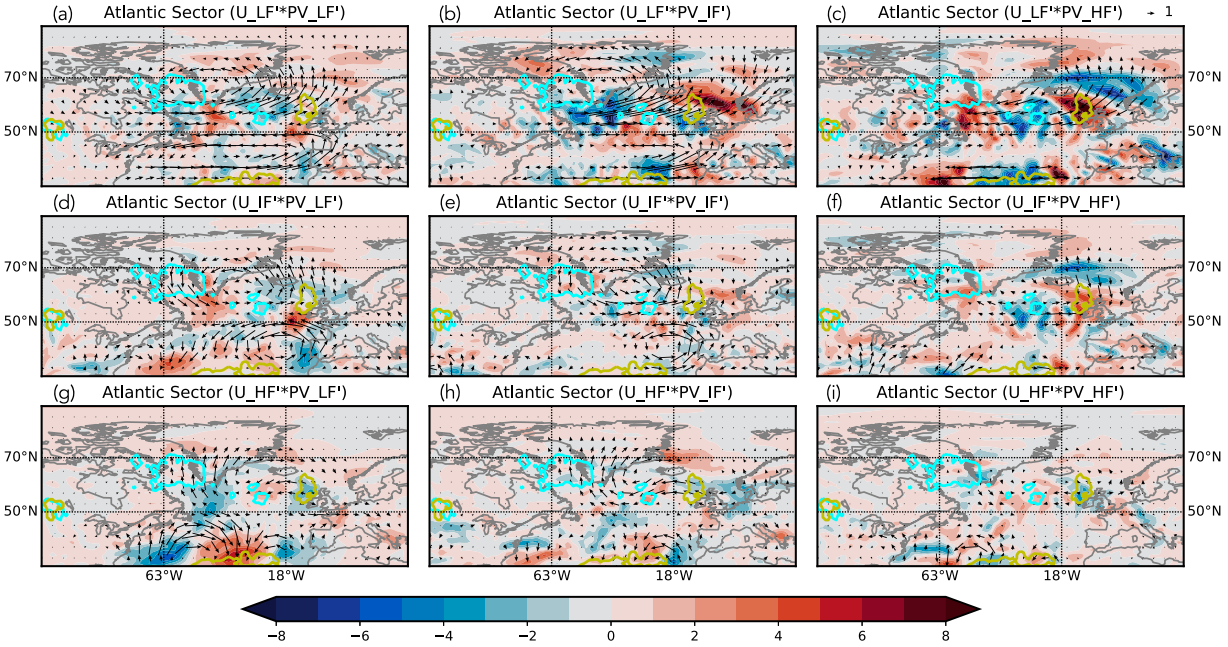

FIG. 8. Atlantic sector 200-hPa horizontal PV flux ($U'q'$; vectors; 10^6 m^3 s^{-2} K kg^{-1}, scale in the top right), PV flux convergence (shading; 10^{12} m^2 K s^{-2} kg^{-1}), locations of anticyclonic (yellow contours) and cyclonic (cyan contours) RWB within 3 days of blocking development for (a) transport of low-frequency (LF) PV by the LF wind, (b) intermediate-frequency (IF) PV by the LF wind, and (c) high-frequency (HF) PV by the LF wind. (d)–(f) As in (a)–(c), but for the decomposed PV fields transported by the IF wind. (g)–(i) As in (a)–(c), but for transport of the decomposed PV fields by the HF winds.

lower latitudes. Madonna et al. (2014) showed this is an average starting location for particles that ascend more than 600–500 hPa in 48 h.

Figure 8 displays the decomposed horizontal PV fluxes and their convergence. The PV flux divergence associated with $\overline{\mathbf{V}_{\mathrm{LF}}q_{\mathrm{IF}}}$ and $\overline{\mathbf{V}_{\mathrm{LF}}q_{\mathrm{HF}}}$ (Figs. 8b,c) contain the strongest magnitudes south and southeast of Greenland. Substantial PV-flux divergence associated with $\overline{\mathbf{V}_{\mathrm{LF}}q_{\mathrm{HF}}}$ is also located in the area of negative PV tendency (Fig. 7a). Additional PV flux divergence is associated with $\overline{\mathbf{V}_{\mathrm{HF}}q_{\mathrm{LF}}}$ south of Greenland (Fig. 8g). Interestingly, despite smaller magnitudes of PV-flux divergence, the most robust PV fluxes are collocated with the cyclonic RWB west of Greenland and are associated with the transport of low-frequency PV anomalies by the low- (Fig. 8a) and intermediate- (Fig. 8d) frequency winds. The results illustrate the importance of the lower-frequency flow component while portraying the multiscale nature of Atlantic blocking events, consistent with Luo et al.'s (2007) finding that planetary-scale waves and synoptic-scale waves force the NAO.

b. *Europe sector*

1) INVESTIGATION OF THE DECOMPOSED Z500 FIELD

The Europe sector blocks (Fig. 9a) contain average low-frequency Z500 variance, while high-frequency flow increases between 4 days and 1 day before onset. An examination of the Z500 field (movie S2) demonstrates a propagating wave train from the North Atlantic to Europe, including a cyclone over Scandinavia on day −3 and cyclogenesis over Greenland before blocking onset. Although a significant decrease of the intermediate variance occurs from day −8 to day −1, the intermediate band contributes to the cyclogenesis over Greenland upstream of the blocking sector (movie S2). The intermediate variance increases sharply from day −1 to day 4 over the blocking sector, indicating the importance of this frequency band in blocking development. Nakamura et al. (1997) stated that a quasi-stationary wave train was of primary importance in European blocking development. However, our results show a traveling wave on the high- and intermediate-Z500 frequency bands.

The ACC between the different frequency bands and the total flow (Fig. 9b) also illustrates the rapid development of the Europe blocking onset as each frequency band shows weak to moderate ACC before day −2. The oscillating ACC for the high-frequency band is associated with the propagating wave train. It is worth noting that blocking onset coincides with the arrival of a high-frequency anomalous high in the blocking sector. The intermediate frequency component strongly resembles the total field after day −2 (i.e., high ACC) and has a larger magnitude than the other two frequency components (movie S2).

2) PV FLUX SCALE INTERACTION, RWB, AND DIABATIC HEATING

The anomalous negative PV tendency before the Europe sector blocking events is centered on the west coast of Scandinavia (Fig. 10a), collocated with the developing blocking high.

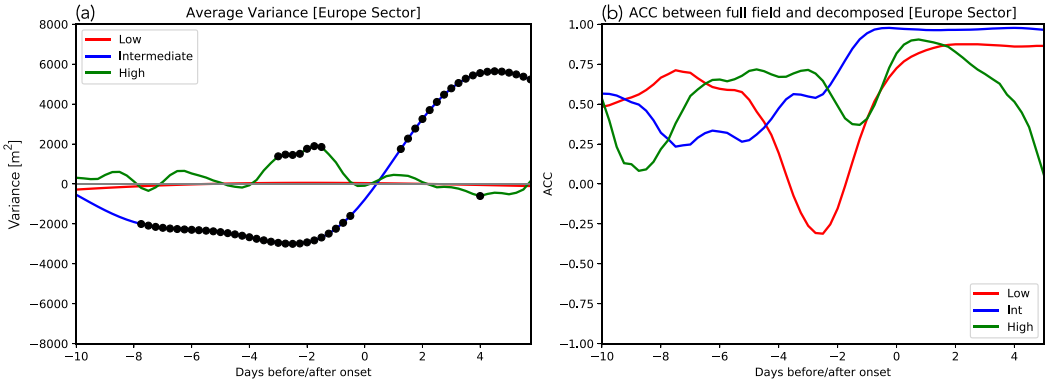

FIG. 9. As in Fig. 6, but for the Europe sector blocking events

The negative PV tendency is associated with an extensive region of enhanced RWB, horizontal and vertical PV flux divergence, and negative diabatic PV tendency (Figs. 10a–d). As stated in section 3, the Europe blocks are manifested as anticyclonic RWB, which would aid in poleward transport of lower-PV air into the blocking domain. The location of anticyclonic RWB occurrence spans from 21°W to about 25°E. Despite the critical role of RWB in Europe blocking, it is worth pointing out that not all RWBs lead to blocking development. Further analysis showed that anticyclonic RWB that occur during Europe blocking events are associated with stronger PV anomalies and are more persistent than those

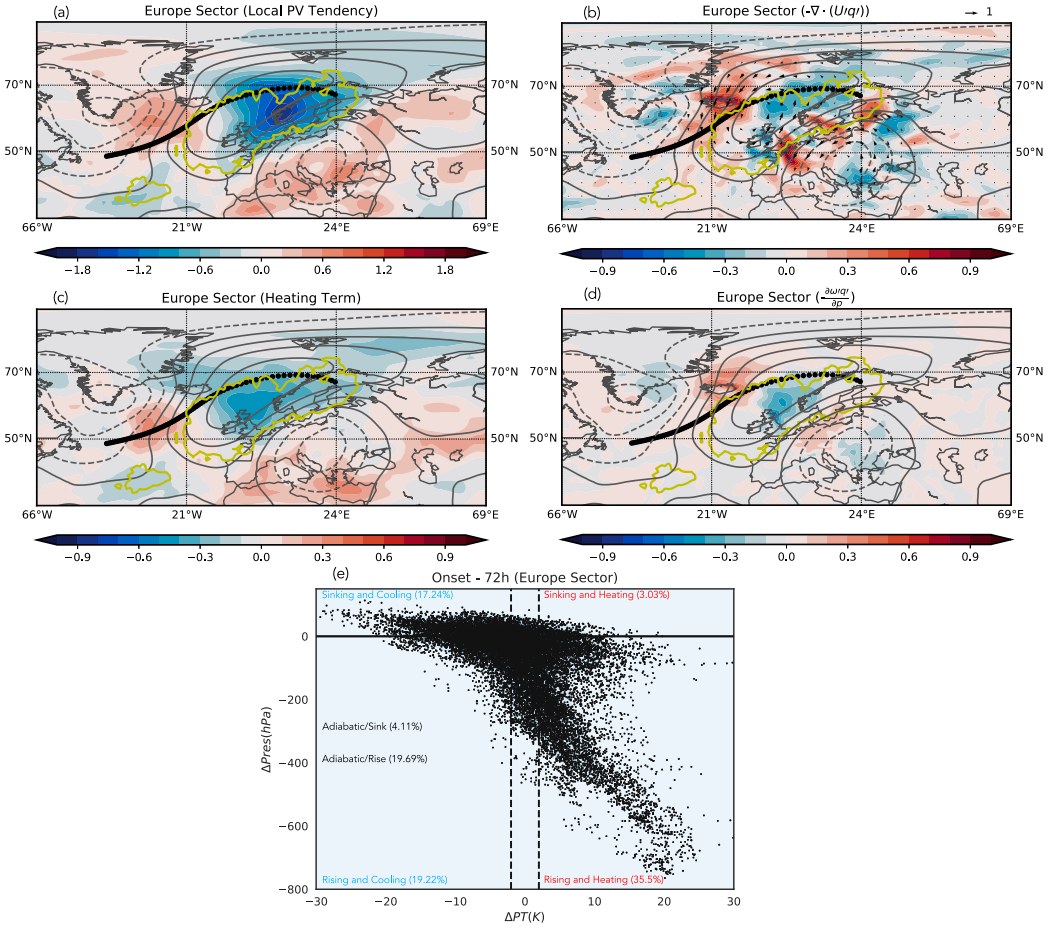

FIG. 10. As in Fig. 7, but for the Europe sector blocking events.

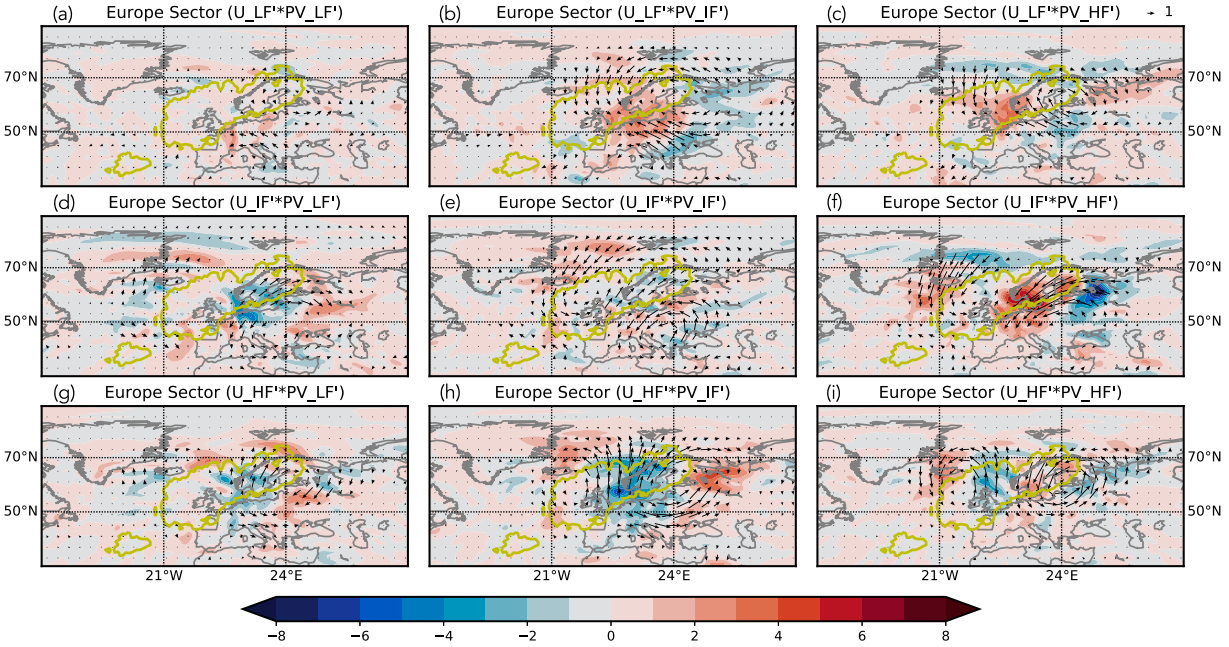

FIG. 11. As in Fig. 8, but for the Europe sector blocking events.

that arise during failed events (Fig. S4). Trajectory analysis shows that ~35% of parcels experience diabatic heating and ascent within 3 days before onset (Fig. 10e), and the average path of this group travels north of the region of anticyclonic RWB (Fig. 10) through the trough–ridge axis (Fig. 3a). This path agrees with Michel et al. (2012), who showed trajectories associated with upstream surface cyclones and anticyclonic RWB before Scandinavian blocking.

The scale interactions involving the low-frequency PV and low-frequency winds (Fig. 11a) are weak, consistent with the weak low-frequency Z500 variance. In contrast, the most substantial PV flux divergence arises from the transport of intermediate-frequency PV by the high-frequency winds ($\overline{\mathbf{V}_{\mathrm{HF}}q_{\mathrm{IF}}}$, Fig. 11h) agreeing with the strong high- and intermediate-frequency Z500 anomalies shown in Fig. 9a and movie S2. This location is collocated with the anomalous negative PV tendency and anticyclonic RWB (Fig. 10a). PV flux divergence is also evident, albeit weaker, associated with $\overline{\mathbf{V}_{\mathrm{IF}}q_{\mathrm{LF}}}$ (Fig. 11d) and $\overline{\mathbf{V}_{\mathrm{HF}}q_{\mathrm{HF}}}$ (Fig. 11i) indicating the important role of high-frequency eddies.

c. *Asian sector*

1) INVESTIGATION OF THE DECOMPOSED Z500 FIELD

The appearance of the stationary wave discussed in section 3 implies influence by lower-frequency dynamics. A gradual buildup in the low-frequency variance is evident for the Asian sector (Fig. 12a), associated with the stationary wave. The low-frequency Z500 pattern at onset (movie S3) resembles the Z500 pattern during strong monsoon winters analyzed by Wang and Chen (2014). Although the intermediate variance is slightly above or even below average before onset, the upstream wave train is associated with strong anomalies on the intermediate-frequency band (movie S3). The intermediate-frequency wave train spans from the western Atlantic to the North Pacific, but it is associated with negative anomalies in the blocking sector before day −4, which transitions to positive anomalies afterward (Fig. 12a). A rapid buildup of the intermediate variance within the blocking sector starts on day −2 and exceeds the variance of the low-frequency band after day 2. Within the blocking sector, the importance of the low- and intermediate-frequency flow components are reiterated by the large ACC with the total flow (Fig. 12b) within 4 days of onset. In contrast, the variance of the high-frequency band is close to the long-term mean from day −10 to day 5 (Fig. 12a).

2) PV FLUX SCALE INTERACTION, RWB, AND DIABATIC HEATING

Figure 13a displays the local PV tendency, with the largest negative tendencies north of 70°N. However, the magnitude of negative PV tendency is much smaller than that over the Atlantic or Europe sector. The circumglobal stationary wave is associated with strong PV fluxes just downstream and poleward of the cyclone located over Europe, contributing to PV flux convergence over Scandinavia and the Barents Sea. The PV flux divergence occurs toward the eastern portion of the negative local PV tendencies (Fig. 13b) along with weak anomalies of vertical PV flux divergence (Fig. 13d). RWB signals are nearly absent in the analysis domain (Fig. 13). The lack of RWB signatures for the Asian sector blocking is consistent with previous studies (Tyrlis and Hoskins 2008; Masato et al. 2012). The percentage of parcels that experience diabatic heating and ascent is the smallest of all blocking sectors (29.9%; Fig. 13e), and the PV anomalies related to the

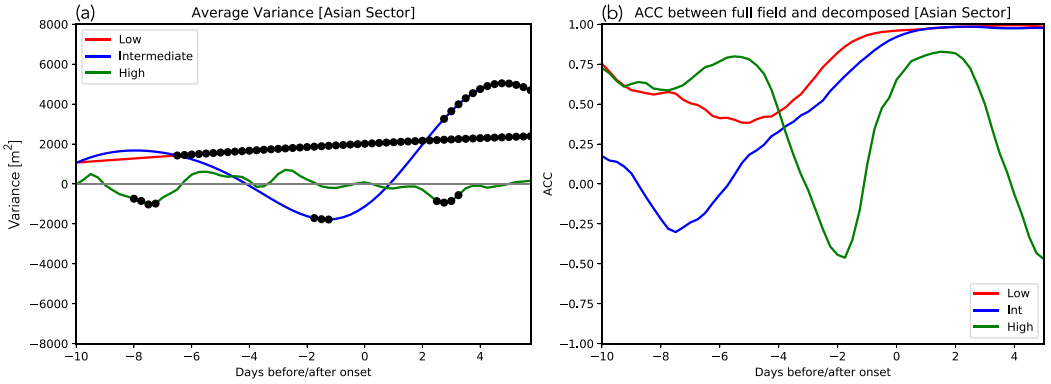

FIG. 12. As in Fig. 6, but for the Asia sector blocking events.

diabatic heating term are also the weakest of all sectors. Still, they are nearly collocated with the negative PV tendency (Fig. 13c). The lack of parcels experiencing heating agrees with Steinfeld and Pfahl (2019), where blocks over land are less influenced by diabatic heating. The Asian sector blocks also contain the largest percentage of parcels that experience isentropic lift (Fig. 13e). The decomposed PV flux terms are not further examined, given the weak PV features associated with the Asian blocks. However, it is important to note that the fluxes associated with PV transport by the high-frequency flow are negligible compared to the low- and intermediate-flow interactions (Fig. S5).

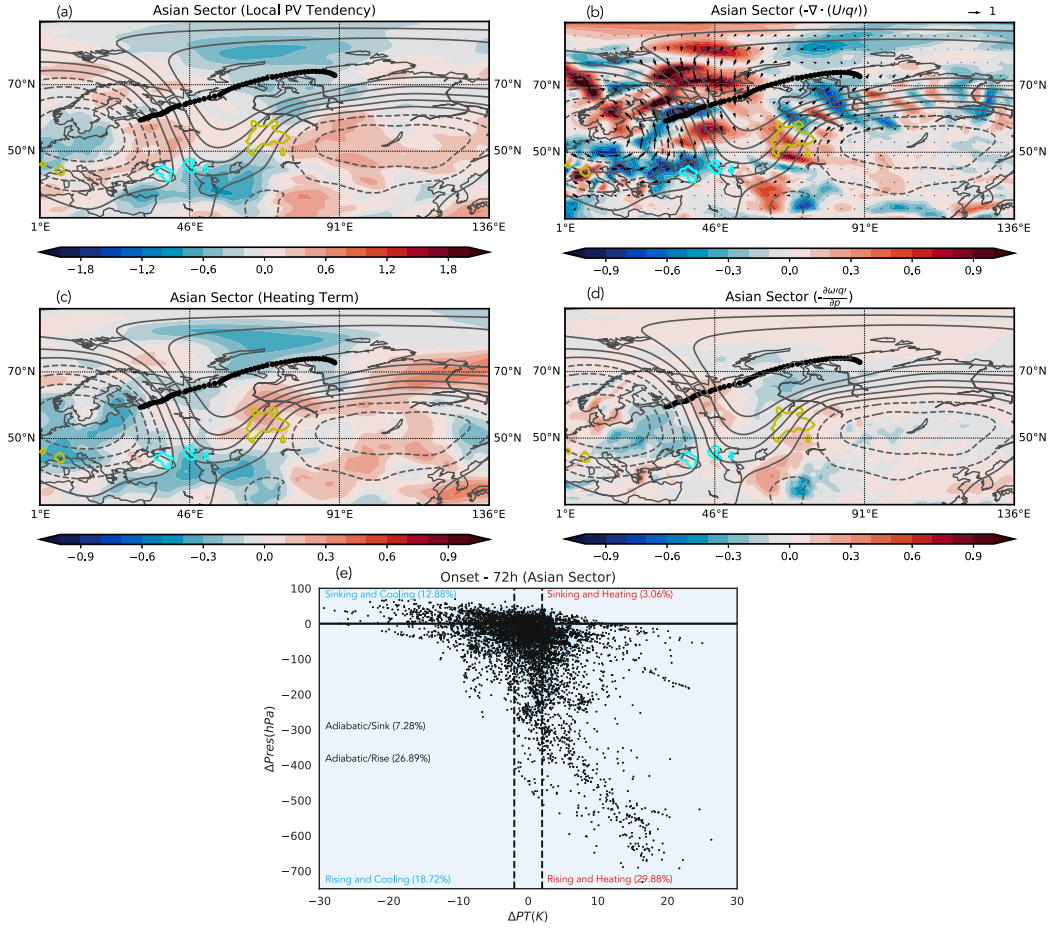

FIG. 13. As in Fig. 7, but for the Asia sector blocking events.

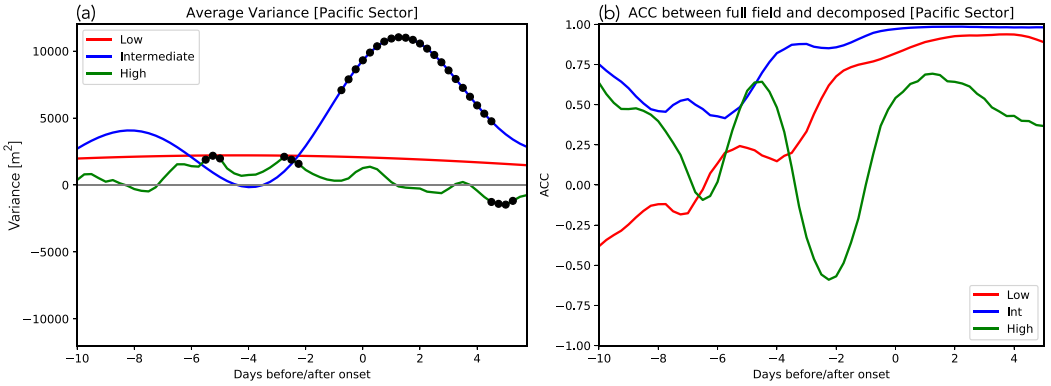

FIG. 14. As in Fig. 6, but for the Pacific sector blocking events

d. Pacific sector

1) INVESTIGATION OF THE DECOMPOSED Z500 FIELD

The Pacific sector contains above-average low-frequency Z500 variance throughout the period, albeit nonsignificant. The high-frequency variance is close to the long-term mean (Fig. 14a). The oscillatory feature of the intermediate variance is associated with the propagation of a wave train, and the intermediate variance becomes dominant from day −2 throughout blocking duration. The flow evolution (movie S4) shows a footprint of the negative Pacific–North American (PNA) pattern within the low-frequency Z500 throughout the 10 days before blocking onset with positive geopotential height anomalies over the North Pacific. There is a known anticorrelation between the PNA and Pacific blocking occurrence (Croci-Maspoli et al. 2007), as the weakened jet during the negative PNA phase produces more favorable blocking conditions. The blocking anticyclone is dominated by the intermediate frequency band, which shows strong anomalies retrogressing across the North Pacific, while high-frequency transient eddies migrate eastward. The importance of the intermediate frequency band is also shown in Fig. 14b. The ACC between the total Z500 field and the intermediate frequency component is larger than the other two frequency bands, especially after day −5. The analysis here, and in Rennert and Wallace (2009), suggests the importance of decomposing the flow into high, intermediate, and low-frequency bands.

2) PV FLUX SCALE INTERACTION, RWB, AND DIABATIC HEATING

Large negative PV tendencies exist just south of Alaska, collocated with the center of the blocking anticyclone (Fig. 15a). Although there are some areas of PV-flux divergence around the center, no divergence occurs in the location of negative local PV tendency. Large equatorward PV fluxes occur toward the western edge of the developing anticyclone, and cyclonic RWB occurs over a large area toward the northwest (Fig. 15b). A small area of anticyclonic RWB occurs within the developing blocking anticyclone. Still, cyclonic RWB plays the more dominant role in poleward transport of negative (low) PV anomalies. The results agree with Masato et al.'s (2012) finding that cyclonic wave breaking is dominant over the North Pacific. The results are also reminiscent of the Atlantic blocks, where negative PV tendency was located downstream of the equatorward PV fluxes. These PV fluxes occur where the block strengthens and retrogresses through formation. Strong vertical PV flux divergence is located toward the eastern portion of the blocking anticyclone (Fig. 15d) and are related to the potential stratospheric precursors discussed in section 3d. The decomposed PV flux terms are not further examined, given the weak contribution of the horizontal PV flux convergence to the PV tendency. However, it is interesting to note that the PV fluxes and associated convergence/divergence related to the flow's intermediate component are strongest (Fig. S6), consistent with the importance of the intermediate frequency of Z500 (Fig. 14 and movie S4).

A large percentage (36%) of parcels experience heating and ascent (Fig. 15e), and the average path 3 days before blocking onset originates just south of Japan (Figs. 15a–d), agreeing with Madonna et al. (2014) as a typical starting location for parcels which ascend along a warm conveyor belt. The Pacific blocks contain the largest percentage of parcels that experience sinking and cooling (Fig. 15e). It is possible that radiative cooling induces negative buoyancy and subsidence (Ferreira et al. 2016; Steinfeld and Pfahl 2019).

5. Summary and discussion

The characteristics and mechanisms of blocking onset over four regions have been analyzed. EOF analysis was performed on the two-dimensional (time × longitude) blocking data, and the leading four EOFs were chosen to represent the four blocking sectors. To study multiscale interaction, the total anomaly fields were decomposed into three frequency bands: high (≤6 days), intermediate (6 < period ≤ 30 days), and low (>30 days), and the PV budget was investigated. Atlantic sector blocking is manifested as the negative phase of the North Atlantic Oscillation and is dominated by low-frequency Z500 and strong cyclonic RWB in the west Atlantic Ocean. The PV budget analysis suggests that both PV flux

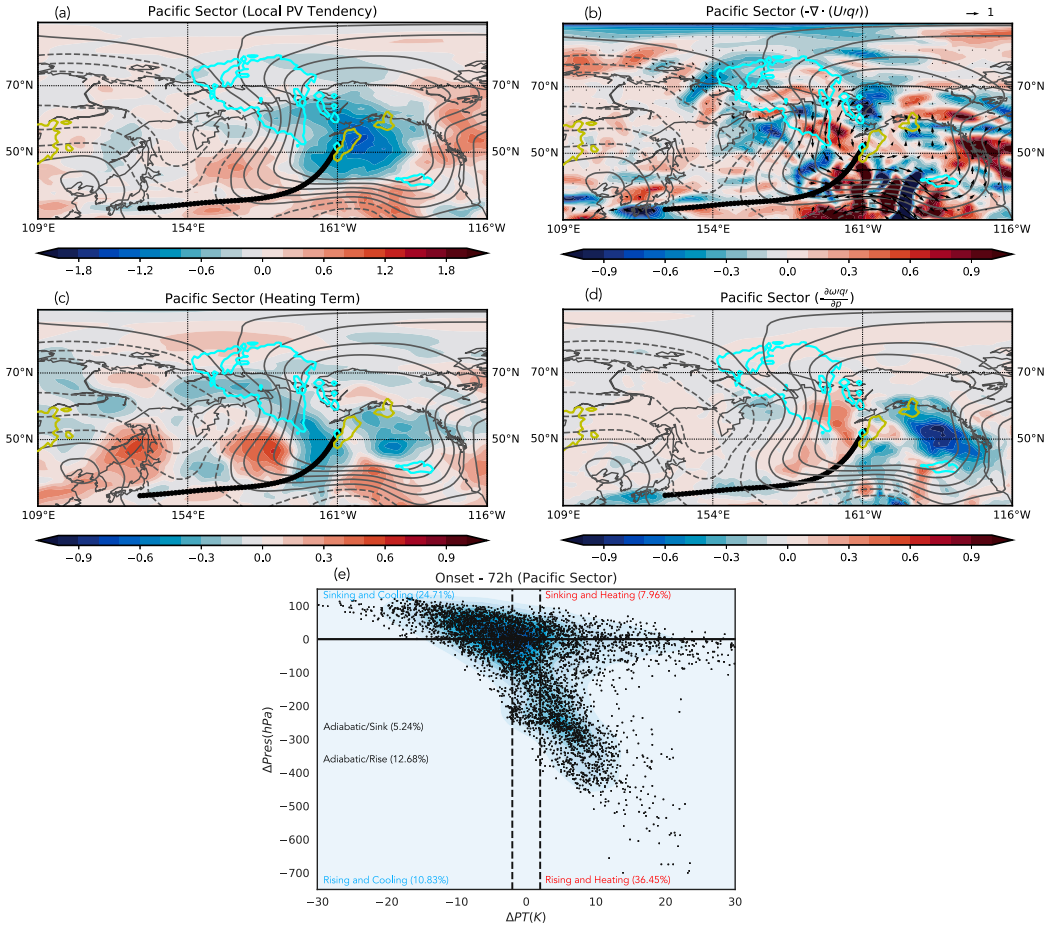

FIG. 15. As in Fig. 7, but for the Pacific sector blocking events.

divergence and diabatic heating contribute to blocking development and possible maintenance. Flow decomposition shows that the strongest PV flux divergence is associated with intermediate- and high-frequency PV transport by the low-frequency winds. Europe sector blocks have a clear anticyclonic wave-breaking signature. Diabatic heating and horizontal/vertical PV flux divergence contribute to the negative PV tendency associated with blocking development. It is shown that Europe sector blocks are strongly influenced by the transport of intermediate- and high-frequency PV by the high-frequency flow. This explains the abrupt nature of blocking onset in this sector but contrasts with Nakamura et al. (1997). They showed that low-frequency dynamics are of primary importance in the formation of Europe blocks. The Asian sector blocks are manifested as a stationary wave train that spans back to the Atlantic Ocean, which is most prominent on the intermediate frequency band. In contrast to the other sectors, the PV features and contribution of diabatic heating to blocking development are weak, and RWB signals are nearly absent. The Pacific blocks are characterized as North Pacific ridging and contain a large area of cyclonic RWB near onset toward the western edge of the anticyclone. The low-frequency component resembles the Pacific–North American (PNA) pattern, but the block is dominated within the intermediate frequency band that is characterized by retrograding waves. Additionally, precursor signals are found in the stratosphere before blocking onset.

This study provides a thorough investigation of mechanisms involved in blocking formation with a specific focus on frequency decomposition, RWB, and diabatic heating, especially how their roles in blocking development differ between different regions. The combination of frequency analysis and Lagrangian-based investigation is novel in its own right. The EOF analysis was used here to identify four geographic sectors objectively. In addition, our work has shown the importance of decomposing the flow into three frequency bands. The importance of including an intermediate frequency component, especially in the cases of Atlantic and Pacific blocks, was made evident. The strong PV fluxes and their divergence that operate across the low and intermediate frequencies are important in blocking initiation for those sectors and failing to include a middle component would miss meaningful scale interactions. An essential question in the literature is how atmospheric blocking will change in the future. Given the different mechanisms for different blocking sectors, the future

changes of blocking may be different across sectors. Another interesting question is whether different onset mechanisms imply different levels of predictability. Both questions demand investigation.

Acknowledgments. This work is supported by the National Oceanic and Atmospheric Administration (NOAA) Grant NA16OAR4310080 and NA18OAR4310271. We acknowledge the NCAR Computational and Information Systems Laboratory (CISL) for providing computing resources. We thank the three anonymous reviewers for enhancing the quality of this manuscript.

Data availability statement. All ERAI data were provided and are available through the Research Data Archive (RDA): https://doi.org/10.5065/D6CR5RD9. The NOAA HYSPLIT model can be run interactively on the READY website: https://www.ready.noaa.gov/HYSPLIT.php.

REFERENCES

Austin, J. F., 1980: The blocking of middle latitude westerly winds by planetary waves. *Quart. J. Roy. Meteor. Soc.*, **106**, 327–350, https://doi.org/10.1002/qj.49710644807.

Barnes, E. A., J. Slingo, and T. Woollings, 2012: A methodology for the comparison of blocking climatologies across indices, models and climate scenarios. *Climate Dyn.*, **38**, 2467–2481, https://doi.org/10.1007/s00382-011-1243-6.

Bell, C. J., L. J. Gray, A. J. Charlton-Perez, and M. M. Joshi, 2009: Stratospheric communication of El Niño teleconnections to European winter. *J. Climate*, **22**, 4083–4096, https://doi.org/10.1175/2009JCLI2717.1.

Benedict, J. J., S. Lee, and S. B. Feldstein, 2004: Synoptic view of the North Atlantic Oscillation. *J. Atmos. Sci.*, **61**, 121–144, https://doi.org/10.1175/1520-0469(2004)061<0121:SVOTNA>2.0.CO;2.

Buehler, T., C. C. Raible, and T. F. Stocker, 2011: The relationship of winter season North Atlantic blocking frequencies to extreme cold or dry spells in the ERA-40. *Tellus*, **63A**, 174–187, https://doi.org/10.1111/j.1600-0870.2010.00492.x.

Cassou, C., L. Terray, and A. S. Phillips, 2005: Tropical Atlantic influence on European heat waves. *J. Climate*, **18**, 2805–2811, https://doi.org/10.1175/JCLI3506.1.

Charney, J. G., and J. G. DeVore, 1979: Multiple flow equilibria in the atmosphere and blocking. *J. Atmos. Sci.*, **36**, 1205–1216, https://doi.org/10.1175/1520-0469(1979)036<1205:MFEITA>2.0.CO;2.

Colucci, S. J., 1985: Explosive cyclogenesis and large-scale circulation changes: Implications of atmospheric blocking. *J. Atmos. Sci.*, **42**, 2701–2717, https://doi.org/10.1175/1520-0469(1985)042<2701:ECALSC>2.0.CO;2.

——, and T. L. Alberta, 1996: Planetary-scale climatology of explosive cyclogenesis and blocking. *Mon. Wea. Rev.*, **124**, 2509–2520, https://doi.org/10.1175/1520-0493(1996)124<2509:PSCOEC>2.0.CO;2.

Croci-Maspoli, M., C. Schwierz, and H. C. Davies, 2007: A multifaceted climatology of atmospheric blocking and its recent linear trend. *J. Climate*, **20**, 633–649, https://doi.org/10.1175/JCLI4029.1.

Davini, P., C. Cagnazzo, R. Neale, and J. Tribbia, 2012: Coupling between Greenland blocking and the North Atlantic Oscillation pattern. *Geophys. Res. Lett.*, **39**, L14701, https://doi.org/10.1029/2012GL052315.

Dee, D. P., and Coauthors, 2011: The ERA-Interim reanalysis: Configuration and performance of the data assimilation system. *Quart. J. Roy. Meteor. Soc.*, **137**, 553–597, https://doi.org/10.1002/qj.828.

Dole, R., and Coauthors, 2011: Was there a basis for anticipating the 2010 Russian heat wave? *Geophys. Res. Lett.*, **38**, L06702, https://doi.org/10.1029/2010GL046582.

Drouard, M., and T. Woollings, 2018: Contrasting mechanisms of summer blocking over western Eurasia. *Geophys. Res. Lett.*, **45**, 12 042–12 048, https://doi.org/10.1029/2018GL079894.

ECMWF, 2009: ERA-Interim project. NCAR RDA CISL, accessed 4 April 2018, https://doi.org/10.5065/D6CR5RD9.

Ferreira, A. P., J. M. Castanheira, and L. Gimeno, 2016: Water vapour stratification and dynamical warming behind the sharpness of the Earth's midlatitude tropopause. *Quart. J. Roy. Meteor. Soc.*, **142**, 957–970, https://doi.org/10.1002/qj.2697.

Hansen, A. R., and T.-C. Chen, 1982: A spectral energetics analysis of atmospheric blocking. *Mon. Wea. Rev.*, **110**, 1146–1165, https://doi.org/10.1175/1520-0493(1982)110<1146:ASEAOA>2.0.CO;2.

——, and A. Sutera, 1993: A comparison between planetary-wave flow regimes and blocking. *Tellus*, **45A**, 281–288, https://doi.org/10.3402/tellusa.v45i4.14892.

Henderson, S. A., E. D. Maloney, and E. A. Barnes, 2016: The influence of the Madden–Julian oscillation on Northern Hemisphere winter blocking. *J. Climate*, **29**, 4597–4616, https://doi.org/10.1175/JCLI-D-15-0502.1.

Hoskins, B. J., 1997: A potential vorticity view of synoptic development. *Meteor. Appl.*, **4**, 325–334, https://doi.org/10.1017/S1350482797000716.

——, M. E. McIntyre, and A. W. Robertson, 1985: On the use and significance of isentropic potential vorticity maps. *Quart. J. Roy. Meteor. Soc.*, **111**, 877–946, https://doi.org/10.1002/qj.49711147002.

Hurrell, J. W., and C. Deser, 2010: North Atlantic climate variability: The role of the North Atlantic Oscillation. *J. Mar. Syst.*, **79**, 231–244, https://doi.org/10.1016/j.jmarsys.2009.11.002.

——, Y. Kushnir, and G. Ottersen, 2003: An overview of the North Atlantic Oscillation. *The North Atlantic Oscillation: Climatic Significance and Environmental Impact*, *Geophys. Monogr.*, Vol. 134, Amer. Geophys. Union, 1–35.

Illari, L., 1984: A diagnostic study of the potential vorticity in a warm blocking anticyclone. *J. Atmos. Sci.*, **41**, 3518–3526, https://doi.org/10.1175/1520-0469(1984)041<3518:ADSOTP>2.0.CO;2.

Ineson, S., and A. Scaife, 2009: The role of the stratosphere in the European climate response to El Niño. *Nat. Geosci.*, **2**, 32–36, https://doi.org/10.1038/ngeo381.

Joos, H., and H. Wernli, 2012: Influence of microphysical processes on the potential vorticity development in a warm conveyor belt: A case-study with the limited-area model COSMO. *Quart. J. Roy. Meteor. Soc.*, **138**, 407–418, https://doi.org/10.1002/qj.934.

Kitano, Y., and T. J. Yamada, 2016: Relationship between atmospheric blocking and cold day extremes in current and RCP8.5 future climate conditions over Japan and the surrounding area. *Atmos. Sci. Lett.*, **17**, 616–622, https://doi.org/10.1002/asl.711.

Kodinariya, T. M., and P. R. Makwana, 2013: Review on determining number of cluster in *k*-means clustering. *Int. J. Adv. Res. Comput. Sci. Manage. Stud.*, **1**, 2321–7782.

Lejenäs, H., and H. Økland, 1983: Characteristics of Northern Hemisphere blocking as determined from a long time series of observational data. *Tellus*, **35A**, 350–362, https://doi.org/10.1111/j.1600-0870.1983.tb00210.x.

Luo, D., 2005: A barotropic envelope Rossby soliton model for block–eddy interaction. Part I: Effect of topography. *J. Atmos. Sci.*, **62**, 5–21, https://doi.org/10.1175/1186.1.

——, and W. Zhang, 2020: A nonlinear multiscale theory of atmospheric blocking: Eastward and upward propagation and energy dispersion of tropospheric blocking wave packets. *J. Atmos. Sci.*, **77**, 4025–4049, https://doi.org/10.1175/JAS-D-20-0153.1.

——, A. R. Lupo, and H. Wan, 2007: Dynamics of eddy-driven low-frequency dipole modes. Part I: A simple model of North Atlantic Oscillations. *J. Atmos. Sci.*, **64**, 3–28, https://doi.org/10.1175/JAS3818.1.

——, J. Cha, L. Zhong, and A. Dai, 2014: A nonlinear multiscale interaction model for atmospheric blocking: The eddy-blocking matching mechanism. *Quart. J. Roy. Meteor. Soc.*, **140**, 1785–1808, https://doi.org/10.1002/qj.2337.

——, W. Zhang, L. Zhong, and A. Dai, 2019: A nonlinear theory of atmospheric blocking: A potential vorticity gradient view. *J. Atmos. Sci.*, **76**, 2399–2427, https://doi.org/10.1175/JAS-D-18-0324.1.

Lupo, A. R., and P. J. Smith, 1995: Climatological features of blocking anticyclones in the Northern Hemisphere. *Tellus*, **47A**, 439–456, https://doi.org/10.3402/tellusa.v47i4.11527.

Madonna, E., H. Wernli, H. Joos, and O. Martius, 2014: Warm conveyor belts in the ERA-Interim dataset (1979–2010). Part I: Climatology and potential vorticity evolution. *J. Climate*, **27**, 3–26, https://doi.org/10.1175/JCLI-D-12-00720.1.

Martin, J. E., 2013: *Mid-Latitude Atmospheric Dynamics: A First Course.* Wiley, 336 pp.

Masato, G., B. J. Hoskins, and T. J. Woollings, 2012: Wave-breaking characteristics of mid-latitude blocking. *Quart. J. Roy. Meteor. Soc.*, **138**, 1285–1296, https://doi.org/10.1002/qj.990.

——, ——, and ——, 2013: Winter and summer Northern Hemisphere blocking in CMIP5 models. *J. Climate*, **26**, 7044–7059, https://doi.org/10.1175/JCLI-D-12-00466.1.

Matsueda, M., 2011: Predictability of Euro-Russian blocking in summer of 2010. *Geophys. Res. Lett.*, **38**, L06801, https://doi.org/10.1029/2010GL046557.

McIntyre, M. E., and T. N. Palmer, 1983: Breaking planetary waves in the stratosphere. *Nature*, **305**, 593–600, https://doi.org/10.1038/305593a0.

Michel, C., and G. Rivière, 2011: The link between Rossby wave breakings and weather regime transitions. *J. Atmos. Sci.*, **68**, 1730–1748, https://doi.org/10.1175/2011JAS3635.1.

——, ——, L. Terray, and B. Joly, 2012: The dynamical link between surface cyclones, upper-tropospheric Rossby wave breaking and the life cycle of the Scandinavian blocking. *Geophys. Res. Lett.*, **39**, L10806, https://doi.org/10.1029/2012GL051682.

Miller, D. E., and Z. Wang, 2019a: Skillful seasonal prediction of Eurasian winter blocking and extreme temperature frequency. *Geophys. Res. Lett.*, **46**, 11 530–11 538, https://doi.org/10.1029/2019GL085035.

——, and ——, 2019b: Assessing seasonal predictability sources and windows of high predictability in the Climate Forecast System, version 2. *J. Climate*, **32**, 1307–1326, https://doi.org/10.1175/JCLI-D-18-0389.1.

——, ——, R. J. Trapp, and D. S. Harnos, 2020: Hybrid prediction of weekly tornado activity out to week 3: Utilizing weather regimes. *Geophys. Res. Lett.*, **47**, e2020GL087253, https://doi.org/10.1029/2020GL087253.

——, ——, B. Li, D. S. Harnos, and T. Ford, 2021: Skillful subseasonal prediction of U.S. extreme warm days and standardized precipitation index in boreal summer. *J. Climate*, **34**, 5887–5898, https://doi.org/10.1175/JCLI-D-20-0878.1.

Nakamura, H., 1994: Rotational evolution of potential vorticity associated with a strong blocking flow configuration over Europe. *Geophys. Res. Lett.*, **21**, 2003–2006, https://doi.org/10.1029/94GL01614.

——, and J. M. Wallace, 1990: Observed changes in baroclinic wave activity during the life cycles of low-frequency circulation anomalies. *J. Atmos. Sci.*, **47**, 1100–1116, https://doi.org/10.1175/1520-0469(1990)047<1100:OCIBWA>2.0.CO;2.

——, and ——, 1993: Synoptic behavior of baroclinic eddies during the blocking onset. *Mon. Wea. Rev.*, **121**, 1892–1903, https://doi.org/10.1175/1520-0493(1993)121<1892:SBOBED>2.0.CO;2.

——, M. Nakamura, and J. L. Anderson, 1997: The role of high- and low-frequency dynamics in blocking formation. *Mon. Wea. Rev.*, **125**, 2074–2093, https://doi.org/10.1175/1520-0493(1997)125<2074:TROHAL>2.0.CO;2.

Nakamura, N., and C. S. Y. Huang, 2018: Atmospheric blocking as a traffic jam in the jet stream. *Science*, **361**, 42–47, https://doi.org/10.1126/science.aat0721.

O'Reilly, C. H., S. Minobe, and A. Kuwano-Yoshida, 2016: The influence of the Gulf Stream on wintertime European blocking. *Climate Dyn.*, **47**, 1545–1567, https://doi.org/10.1007/s00382-015-2919-0.

Peings, Y., and G. Magnusdottir, 2014: Forcing of the wintertime atmospheric circulation by the multidecadal fluctuations of the North Atlantic Ocean. *Environ. Res. Lett.*, **9**, 034018, https://doi.org/10.1088/1748-9326/9/3/034018.

Pelly, J. L., and B. J. Hoskins, 2003: A new perspective on blocking. *J. Atmos. Sci.*, **60**, 743–755, https://doi.org/10.1175/1520-0469(2003)060<0743:ANPOB>2.0.CO;2.

Pfahl, S., C. Schwierz, M. Croci-Maspoli, C. M. Grams, and H. Wernli, 2015: Importance of latent heat release in ascending air streams for atmospheric blocking. *Nat. Geosci.*, **8**, 610–614, https://doi.org/10.1038/ngeo2487.

Pomroy, H. R., and A. J. Thorpe, 2000: The evolution and dynamical role of reduced upper-tropospheric potential vorticity in intensive observing period one of FASTEX. *Mon. Wea. Rev.*, **128**, 1817–1834, https://doi.org/10.1175/1520-0493(2000)128<1817:TEADRO>2.0.CO;2.

Reinhold, B. B., and R. T. Pierrehumbert, 1982: Dynamics of weather regimes: Quasi-stationary waves and blocking. *Mon. Wea. Rev.*, **110**, 1105–1145, https://doi.org/10.1175/1520-0493(1982)110<1105:DOWRQS>2.0.CO;2.

Rennert, K. J., and J. M. Wallace, 2009: Cross-frequency coupling, skewness, and blocking in the Northern Hemisphere winter circulation. *J. Climate*, **22**, 5650–5666, https://doi.org/10.1175/2009JCLI2669.1.

Rex, D., 1950: Blocking action in the middle troposphere and its effect on regional climate. I: An aerological study of blocking. *Tellus*, **2**, 196–211, https://doi.org/10.3402/tellusa.v2i3.8546.

Scaife, A. A., J. R. Knight, G. K. Vallis, and C. K. Folland, 2005: A stratospheric influence on the winter NAO and North Atlantic surface climate. *Geophys. Res. Lett.*, **32**, L18715, https://doi.org/10.1029/2005GL023226.

Shutts, G. J., 1983: The propagation of eddies in diffluent jetstreams: Eddy vorticity forcing of 'blocking' flow fields. *Quart. J. Roy. Meteor. Soc.*, **109**, 737–761, https://doi.org/10.1002/qj.49710946204.

Sillmann, J., and M. Croci-Maspoli, 2009: Present and future atmospheric blocking and its impact on European mean and extreme climate. *Geophys. Res. Lett.*, **36**, L10702, https://doi.org/10.1029/2009GL038259.

——, ——, M. Kallache, and R. Katz, 2011: Extreme cold winter temperatures in Europe under the influence of North Atlantic atmospheric blocking. *J. Climate*, **24**, 5899–5913, https://doi.org/10.1175/2011JCLI4075.1.

Stein, A. F., R. R. Draxler, G. D. Rolph, B. J. Stunder, M. D. Cohen, and F. Ngan, 2015: NOAA's HYSPLIT atmospheric transport and dispersion modeling system. *Bull. Amer. Meteor. Soc.*, **96**, 2059–2077, https://doi.org/10.1175/BAMS-D-14-00110.1.

Steinfeld, D., and S. Pfahl, 2019: The role of latent heating in atmospheric blocking dynamics: A global climatology. *Climate Dyn.*, **53**, 6159–6180, https://doi.org/10.1007/s00382-019-04919-6.

Stoelinga, M. T., 1996: A potential vorticity–based study of the role of diabatic heating and friction in a numerically simulated baroclinic cyclone. *Mon. Wea. Rev.*, **124**, 849–874, https://doi.org/10.1175/1520-0493(1996)124<0849:APVBSO>2.0.CO;2.

Strong, C., and G. Magnusdottir, 2008: Tropospheric Rossby wave breaking and the NAO/NAM. *J. Atmos. Sci.*, **65**, 2861–2876, https://doi.org/10.1175/2008JAS2632.1.

Swanson, K. L., 2001: Blocking as a local instability to zonally varying flows. *Quart. J. Roy. Meteor. Soc.*, **127**, 1341–1355, https://doi.org/10.1002/qj.49712757412.

Swenson, E. T., and D. M. Straus, 2017: Rossby wave breaking and transient eddy forcing during Euro-Atlantic circulation regimes. *J. Atmos. Sci.*, **74**, 1735–1755, https://doi.org/10.1175/JAS-D-16-0263.1.

Tibaldi, S., and F. Molteni, 1990: On the operational predictability of blocking. *Tellus*, **42A**, 343–365, https://doi.org/10.3402/tellusa.v42i3.11882.

Toniazzo, T., and A. A. Scaife, 2006: The influence of ENSO on winter North Atlantic climate. *Geophys. Res. Lett.*, **33**, L24704, https://doi.org/10.1029/2006GL027881.

Tyrlis, E., and B. J. Hoskins, 2008: Aspects of a Northern Hemisphere atmospheric blocking climatology. *J. Atmos. Sci.*, **65**, 1638–1652, https://doi.org/10.1175/2007JAS2337.1.

Wang, L., and W. Chen, 2014: An intensity index for the East Asian winter monsoon. *J. Climate*, **27**, 2361–2374, https://doi.org/10.1175/JCLI-D-13-00086.1.

Wernli, B. H., and H. C. Davies, 1997: A Lagrangian-based analysis of extratropical cyclones. I: The method and some applications. *Quart. J. Roy. Meteor. Soc.*, **123**, 467–489, https://doi.org/10.1002/qj.49712353811.

Wilks, D. S., 2011: *Statistical Methods in the Atmospheric Sciences*. 3rd ed. Academic Press, 704 pp.

——, 2016: "The stippling shows statistically significant grid points": How research results are routinely overstated and overinterpreted, and what to do about it. *Bull. Amer. Meteor. Soc.*, **97**, 2263–2273, https://doi.org/10.1175/BAMS-D-15-00267.1.

Woollings, T., B. Hoskins, M. Blackburn, and P. Berrisford, 2008: A new Rossby wave-breaking interpretation of the North Atlantic Oscillation. *J. Atmos. Sci.*, **65**, 609–626, https://doi.org/10.1175/2007JAS2347.1.

——, and Coauthors, 2018: Blocking and its response to climate change. *Curr. Climate Change Rep.*, **4**, 287–300, https://doi.org/10.1007/s40641-018-0108-z.

Yamamoto, A., M. Nonaka, P. Martineau, A. Yamazaki, Y. O. Kwon, H. Nakamura, and B. Taguchi, 2021: Oceanic moisture sources contributing to wintertime Euro-Atlantic blocking. *Wea. Climate Dyn.*, **2**, 819–840, https://doi.org/10.5194/wcd-2-819-2021.